nature methods

Article

https://doi.org/10.1038/s41592-023-02020-9

Fatigue-resistant hydrogel optical fibers enable peripheral nerve optogenetics during locomotion

Received: 28 March 2022

Accepted: 21 August 2023

Published online: 19 October 2023

Check for updates

Xinyue Liu[1,2,17] ✉, Siyuan Rao[3,16,17] ✉, Weixuan Chen[3], Kayla Felix[3], Jiahua Ni[1], Atharva Sahasrabudhe[4,5,6], Shaoting Lin[1,7], Qianbin Wang[3,16], Yuanyuan Liu[8], Zhigang He[9,10], Jingyi Xu[3], Sizhe Huang[3,16], Eunji Hong[3,16], Todd Yau[11], Polina Anikeeva[4,5,12,13,14,17] ✉ & Xuanhe Zhao[1,15,17] ✉

We develop soft and stretchable fatigue-resistant hydrogel optical fibers that enable optogenetic modulation of peripheral nerves in naturally behaving animals during persistent locomotion. The formation of polymeric nanocrystalline domains within the hydrogels yields fibers with low optical losses of 1.07 dB cm^{-1}, Young's modulus of 1.6 MPa, stretchability of 200% and fatigue strength of 1.4 MPa against 30,000 stretch cycles. The hydrogel fibers permitted light delivery to the sciatic nerve, optogenetically activating hindlimb muscles in Thy1::ChR2 mice during 6-week voluntary wheel running assays while experiencing repeated deformation. The fibers additionally enabled optical inhibition of pain hypersensitivity in an inflammatory model in TRPV1::NpHR mice over an 8-week period. Our hydrogel fibers offer a motion-adaptable and robust solution to peripheral nerve optogenetics, facilitating the investigation of somatosensation.

Optogenetics has transformed the field of systems neuroscience by allowing precise control over the activity of specific cell populations[1,2]. While it is routinely applied to the study of brain circuits, the application of optogenetic modulation to peripheral nerves that undergo vigorous motion remains challenging (Fig. 1a,b)[3,4]. Light delivery devices composed of rigid materials, such as silica fibers, with GPa moduli can damage soft tissues with moduli in kPa to MPa range upon repeated deformation and displacement[5,6]. Additionally, implanting rigid devices within extremities may impede natural animal behaviors. Although flexible devices with microscale light-emitting diodes created through microfabrication are suitable for stimulating peripheral nerves and the spinal cord in freely moving rodents, their sophisticated

[1]Department of Mechanical Engineering, Massachusetts Institute of Technology, Cambridge, MA, USA. [2]Department of Chemical Engineering and Materials Science, Michigan State University, East Lansing, MI, USA. [3]Department of Biomedical Engineering, University of Massachusetts Amherst, Amherst, MA, USA. [4]Research Laboratory of Electronics, Massachusetts Institute of Technology, Cambridge, MA, USA. [5]McGovern Institute for Brain Research, Massachusetts Institute of Technology, Cambridge, MA, USA. [6]Department of Chemistry, Massachusetts Institute of Technology, Cambridge, MA, USA. [7]Department of Mechanical Engineering, Michigan State University, East Lansing, MI, USA. [8]Somatosensation and Pain Unit, National Institute of Dental and Craniofacial Research, National Center for Complementary and Integrative Health, National Institutes of Health, Bethesda, MD, USA. [9]F.M. Kirby Neurobiology Center, Boston Children's Hospital, Harvard Medical School, Boston, MA, USA. [10]Department of Neurology, Harvard Medical School, Boston, MA, USA. [11]Department of Biochemistry and Molecular Biology, University of Massachusetts Amherst, Amherst, MA, USA. [12]Department of Materials Science and Engineering, Massachusetts Institute of Technology, Cambridge, MA, USA. [13]Department of Brain and Cognitive Sciences, Massachusetts Institute of Technology, Cambridge, MA, USA. [14]K. Lisa Yang Brain-Body Center, Massachusetts Institute of Technology, Cambridge, MA, USA. [15]Department of Civil and Environmental Engineering, Massachusetts Institute of Technology, Cambridge, MA, USA. [16]Present address: Department of Biomedical Engineering, Binghamton University, State University of New York, Binghamton, NY, USA. [17]These authors contributed equally: Xinyue Liu, Siyuan Rao, Polina Anikeeva, Xuanhe Zhao. ✉e-mail: xyliu@msu.edu; syrao@binghamton.edu; anikeeva@mit.edu; zhaox@mit.edu

design presents implementation challenges outside of specialized facilities[7–10]. More notably, vigorous and repeated deformation during locomotion may accelerate fatigue failures at rigid–soft interfaces within microfabricated devices, resulting in reduced efficacy and reliability of neuromodulation over time[11].

Optical fibers offer precise spatial targeting, scalable manufacturing and facile coupling to commercial light sources[12–14]. Fibers composed of polymers, such as polycarbonate, polymethyl methacrylate, polystyrene and cyclic olefin copolymer, enabled optogenetic stimulation in the mouse gut lumen and spinal cord[14,15]. However, the moduli in the GPa range and limited elasticity have hindered applications of polymer fibers in peripheral nerves experiencing large deformations (Extended Data Fig. 1a,b)[3,15,16]. Due to their optical transparency in the visible range and tunable mechanics, hydrogels are a promising platform for delivering light to mobile peripheral nerves[17–21]. However, a number of technical challenges have precluded their effective implementation as optical nerve interfaces. The available hydrogel materials are susceptible to fatigue fracture from recurring deformations during animal locomotion (Extended Data Fig. 1c)[6,20,22]. The coupling of light into hydrogel fibers typically relies on rigid–soft interfaces between silica and hydrogels that are vulnerable to fatigue fracture during repeated mechanical loading[23]. Furthermore, the low refractive indices of fully hydrated hydrogels (~1.34) and poor refractive index contrast between the core and cladding materials lead to severe light leakage along the hydrogel fibers[20].

Here we present fatigue-resistant hydrogel optical fibers that adapt to persistent locomotion in naturally behaving mice (Fig. 1c). Polymeric nanocrystalline domains were introduced within the hydrogel fibers, which prevented crack propagation and ensured fiber resilience against repeated stretching (Fig. 1d). Nanocrystalline domains were also generated at the silica–hydrogel interface to establish a robust light coupling with an external light source through a commercial silica fiber segment (Fig. 1d). Additionally, the hydrogel fibers were equipped with a cuff at their distal end to facilitate robust contact with peripheral nerves during deformation (Fig. 1e and Extended Data Fig. 1d). In chronic voluntary wheel running assays, the hydrogel fibers delivered blue light to the sciatic nerves, allowing optogenetic stimulation of hindlimb muscles in Thy1::ChR2-EYFP mice, which broadly express the blue-light-sensitive cation channel channelrhodopsin 2 (ChR2) fused to an enhanced yellow fluorescent protein (EYFP) in their nervous systems. This technology was also applied to TRPV1::NpHR-EYFP mice, which express the yellow-light-gated chloride pump halorhodopsin (NpHR) fused to EYFP in primary sensory afferents. In an inflammatory pain model, optical pulses delivered through the implanted hydrogel fibers to sciatic nerves yielded NpHR-mediated inhibition of pain hypersensitivity over an 8-week study.

Results

Fabrication of fatigue-resistant hydrogel optical fibers

To facilitate light delivery to the peripheral nervous system, we designed a hydrogel-based device that consists of a short silica segment to prevent hydrogel dehydration in air, a polyvinyl alcohol (PVA) hydrogel fiber with a core–cladding structure and a hydrogel cuff attached to the targeted nerve (Fig. 1c). An amorphous PVA hydrogel core was first chemically crosslinked within a tubular mold and directly connected to a short silica segment. Next, we converted the amorphous polymers to nanocrystalline domains to resist crack propagation at the silica–hydrogel interface and in the bulk hydrogel through annealing (Fig. 1d and Extended Data Fig. 2a,b). The presence of PVA nanocrystalline domains not only improved the hydrogel core's refractive index but also ensured a durable silica–hydrogel connection to minimize light loss. After annealing and rehydration, the hydrogel core was 600 µm in diameter and 6 cm in length. To prevent light leakage from the hydrogel core and thus avoid off-target illumination, we fabricated an amorphous hydrogel cladding (thickness: 200 µm) around the crystalline hydrogel core. During cladding synthesis, a light-absorbing nanomaterial, reduced graphene oxide (rGO, 0.21 wt%), was incorporated within an amorphous PVA hydrogel[24]. The PVA polymer chains at the hydrogel core–cladding interface interpenetrated and formed hydrogen bonds to ensure strong adhesion (Fig. 1e and Extended Data Fig. 2c). To create robust and flexible contact with the targeted nerve, a hydrogel cuff was fabricated at the fiber distal end (Fig. 1e).

Optical characterization of undeformed hydrogel fibers

For effective light delivery with minimal light loss, we first engineered the light absorption and scattering in the PVA hydrogel core by controlling the growth of nanocrystalline domains. Wide-angle X-ray scattering (WAXS) analysis revealed that 30-min annealing generates nanocrystalline domains with an average size (d_{nd}) of 3.9 nm, which is two orders of magnitude smaller than the selected light wavelengths (λ = 473 nm for ChR2 activation and 589 nm for NpHR activation) (Fig. 1f and Extended Data Fig. 3a–c)[6,25]. The resultant PVA hydrogel material exhibited low light absorbance (Fig. 1g). Extended annealing time and reduced chemical crosslinking generated more nanocrystalline domains, leading to structural heterogeneity in hydrogels and increased light absorbance (Extended Data Fig. 3b–i).

Refractive index contrast between the hydrogel core (n_{core}) and cladding ($n_{cladding}$) can efficiently confine the light transmission within the hydrogel core. Therefore, we optimized their refractive indices by choosing the nanocrystalline PVA as the hydrogel core (n_{core} = 1.380), and amorphous PVA as the hydrogel cladding ($n_{cladding}$ = 1.342) (Fig. 1h,i). Compared with amorphous hydrogels, nanocrystalline hydrogels exhibit a higher refractive index due to the lower water content and more densely packed nanocrystalline domains[20,26]. Ray tracing simulations confirmed that the increased contrast of refractive indices reduces light leakage (Extended Data Fig. 3j,k). The light intensity collected from amorphous PVA hydrogel fibers is only 17% of that collected from nanocrystalline PVA hydrogel fibers of the same length (Extended Data Fig. 3l,m). To further reduce light leakage, the hydrogel cladding was designed to be light-absorbing. A 200-µm-thick cladding made of amorphous rGO-PVA was generated with low light transmittances of 4.2% at 473 nm and 13.1% at 589 nm (Extended Data Fig. 3n–q).

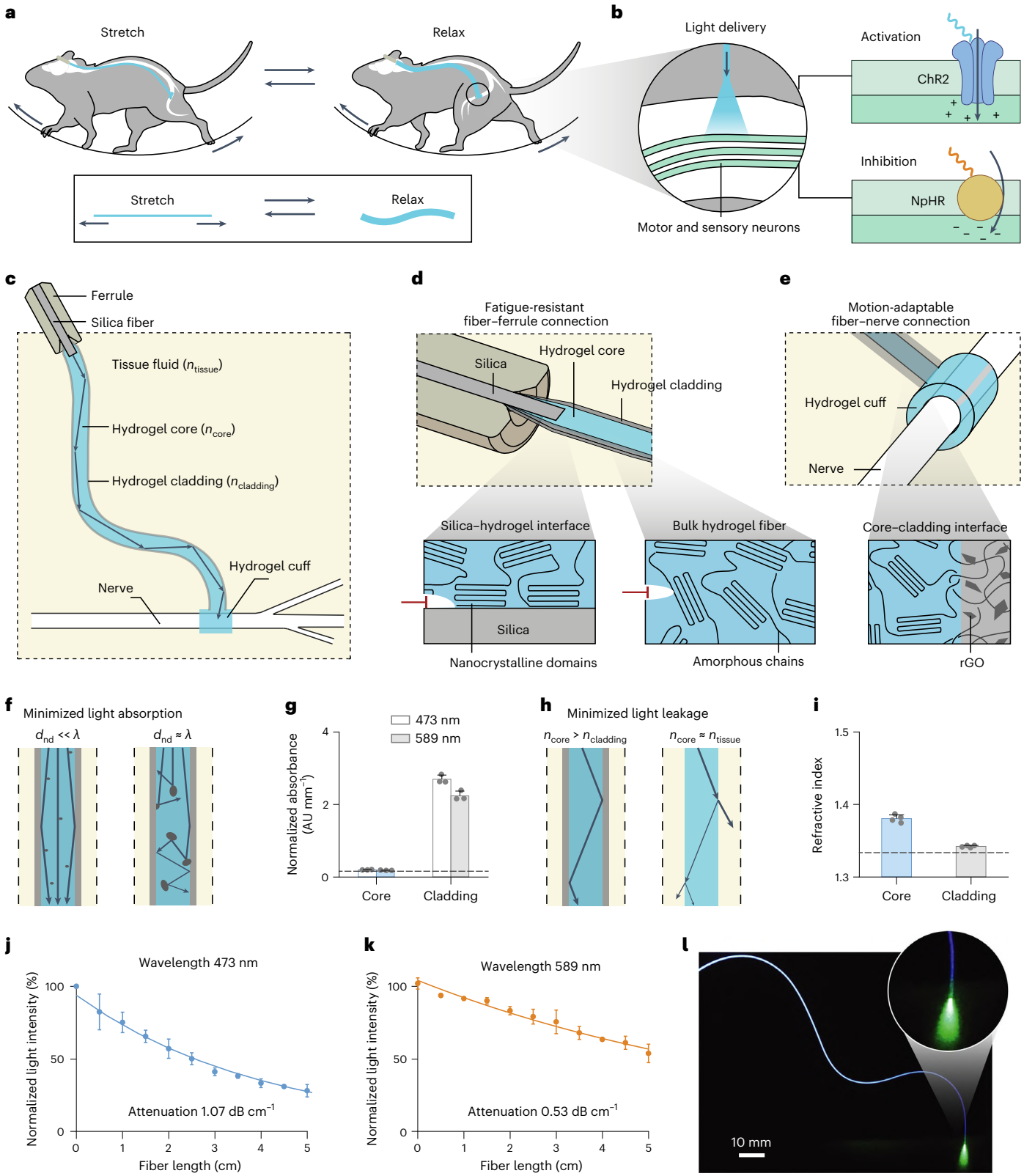
Fig. 1 | Design and mechanisms of hydrogel optical fibers. a, Schematics of hydrogel fibers implanted under the skin used for light delivery to peripheral nerves and the repeated stretching they experience during animal locomotion. **b**, Optogenetic activation or inhibition of motor and sensory neurons expressing opsins (for example, ChR2 and NpHR) in peripheral nerves via a hydrogel fiber. **c**, Schematic of a hydrogel fiber composed of a short silica fiber in a ceramic optic ferrule, a hydrogel core, a hydrogel cladding and a hydrogel cuff in the tissue fluid. **d**, Hydrogel core material adheres to a short silica fiber, enabling the fatigue-resistant connection between the ferrule and fiber. **e**, Hydrogel cuff wrapped around a targeted nerve, enabling the motion-adaptable connection between the nerve and fiber. The hydrogel core–cladding interface is achieved by polymer chain interpenetration. **f**, Hydrogel core material contains nanocrystalline domains (d_{nd}) that are much smaller than the light wavelength (λ), enabling minimized light absorption and scattering. **g**, Normalized absorbance at 473 nm and 589 nm for the hydrogel core and hydrogel cladding materials. The dashed line represents the absorbance of PBS. AU, absorbance units. **h**, Hydrogel core material exhibits a higher refractive index than that of the hydrogel cladding material and tissue fluid, enabling minimized light leakage at the core–cladding interface. **i**, Refractive index for the hydrogel core and cladding materials. The dashed line represents the refractive index of PBS. **j**,**k**, Plot of normalized light intensity versus fiber length at 473 nm (**j**) and 589 nm (**k**). The measured attenuation coefficients are 1.07 dB cm^{-1} at 473 nm and 0.53 dB cm^{-1} at 589 nm. **l**, Representative image of blue-light delivery through a deformed hydrogel fiber (no cladding and cuff). The inset is the magnified image of the fiber distal end directed to a calcein acetoxymethyl ester solution. Scale bar, 10 mm.

https://doi.org/10.1038/s41592-023-02020-9

The resulting hydrogel fibers exhibited light attenuation coefficients of 1.07 dB cm^{-1} at 473 nm and 0.53 dB cm^{-1} at 589 nm in the fully hydrated state (Fig. 1j,k). The optical performance remained stable even when incubated in the physiological conditions for 6 months (1.09 ± 0.22 dB cm^{-1} at 473 nm; Extended Data Fig. 3r). These attenuation coefficients are comparable to those seen in polymer fibers with GPa moduli[14,15]. When coupled to a light source (input: 45 mW) (Fig. 1l), light delivered through a 6-cm-long hydrogel fiber is sufficient to trigger ChR2-mediated neuronal excitation (output: 35.4 mW mm^{-2}) (refs. 27–29).

Optical characterization of deformed hydrogel fibers

We evaluated whether hydrogel fibers can maintain adequate light transmission during mechanical deformation. The hydrogel fibers



https://doi.org/10.1038/s41592-023-02020-9

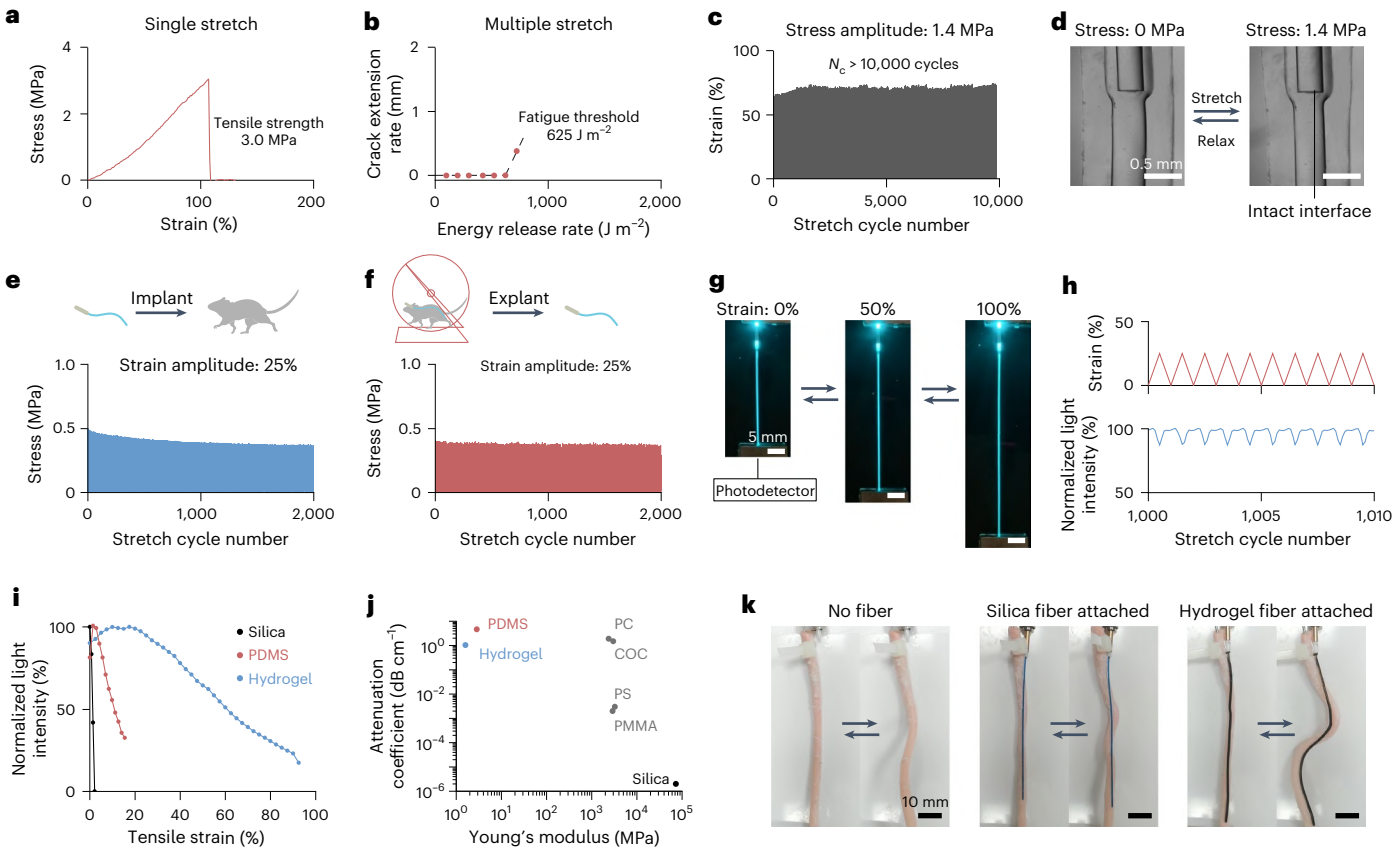


Fig. 2 | Mechanical robustness and flexibility of hydrogel optical fibers. a, Representative plot of nominal stress versus strain of the hydrogel fiber under single-cycle tensile test. The measured tensile strength is 3.0 MPa and Young's modulus is 1.6 MPa. **b**, Plot of crack extension rate versus energy release rate of the hydrogel–silica interface under cyclic peeling test. The measured interfacial fatigue threshold is 625 J m^{-2}. **c**, Plot of strain versus cycle number of the hydrogel fiber under cyclic tensile test. The applied stress amplitude in the cyclic tensile test is 1.4 MPa and the total cycle number (N_c) is larger than 10,000. **d**, Microscopic images of the hydrogel fiber at different tensile stresses under cyclic tensile test. Scale bars, 0.5 mm. **e**,**f**, Representative plots of stress versus cycle number of the hydrogel fiber under cyclic tensile test before implantation (**e**) and after 8-week implantation (**f**). The applied strain amplitudes are 25%. **g**, Images of the hydrogel fiber (no cladding) at different tensile strains with the two ends connected to a light source and a photodetector, respectively. Scale bars, 5 mm. **h**, Representative plots of strain and normalized light intensity versus cycle number of the hydrogel fiber. **i**, Representative plot of normalized light intensity versus tensile strain of the silica, PDMS and hydrogel fibers in PBS. **j**, Comparison of the attenuation coefficient and Young's modulus of the hydrogel fiber and various transparent materials, including silica, PDMS, polymethyl methacrylate (PMMA), polystyrene (PS), cyclic olefin copolymer (COC) and polycarbonate (PC). **k**, Images of a porcine artery with no fiber, an artery with a silica fiber attached and an artery with a hydrogel fiber attached. Scale bars, 10 mm.

possess a Young's modulus of 1.6 MPa, tensile strength of 3.0 MPa and stretchability of 200% during a single-cycle tensile test (Fig. 2a and Extended Data Fig. 4a). This Young's modulus is 3–4 orders of magnitude lower than that of silica fibers (73 GPa) and previously reported polymer fibers (2.0 GPa for polycarbonate, 2.9 GPa for polymethyl methacrylate and 2.6 GPa for cyclic olefin copolymer)[14,30], improving mechanical matching with biological tissues such as muscle (0.02 MPa) and sciatic nerve (0.6 MPa)[6,31]. To assess the fatigue resistance of the hydrogel fibers under physiological conditions, we subjected them to repeated mechanical loading in phosphate-buffered saline (PBS). The fatigue threshold of the silica–hydrogel interface was measured to be 625 J m^{-2}, comparable to the interfacial fatigue threshold found in the natural cartilage–bone interface (800 J m^{-2}) (Fig. 2b and Extended Data Fig. 4b). Commensurate with the loading frequency and mechanical strength of load-bearing muscles, we performed cyclic tensile tests on the hydrogel fibers with a frequency of 1 Hz and stress amplitude of 1.4 MPa (refs. 32,33). These cyclic tests revealed that the maximum strain maintained ~70% over 10,000 cycles with no cavity or crack formation at the silica–hydrogel interface (Fig. 2c,d). In addition, the hydrogel fibers exhibited resilience (0% hysteresis) and low modulus (1.6 MPa) even after cyclic loading (Extended Data Fig. 4c). By performing cyclic stretching with different stress amplitudes, we determined the 30,000-cycle fatigue strength to be 1.4 MPa, similar to the strength of skeletal muscles (0.4–2.0 MPa) (Extended Data Fig. 4d–f)[34]. Notably, no changes in mechanical behaviors were observed following their 8-week implantation in mice or 6-month incubation in PBS (Fig. 2e,f and Extended Data Fig. 4g,h).

We further investigated the optical transmission of the hydrogel fibers under cyclic stretching at a frequency of 1 Hz and a strain amplitude of 25%, which mimicked the mechanical loading occurring during locomotion (Fig. 2g)[35]. We found that the hydrogel fibers maintained light transmission above 87% for more than 1,000 stretch cycles (Fig. 2g,h and Supplementary Video 1). We subsequently evaluated the light transmission under extreme tensile loading. The hydrogel fiber transmitted 23% of maximum light intensity, even when elongated at a strain of 90%. Unlike stretchable hydrogel fibers, the silica fiber fractured at a strain of 1% and the polydimethylsiloxane (PDMS) fiber failed at a strain of 20% due to their low fracture energies (Fig. 2i)[36,37]. We also measured the light transmission of different optical fibers under bending (Extended Data Fig. 4i). Compared with common fiber materials, the hydrogel fibers showed high mechanical compliance and relatively low optical losses (Fig. 2j)[38].

We also tested their adaptability to physiological tissue motion by attaching the fibers to a porcine artery ex vivo and simulating tissue

https://doi.org/10.1038/s41592-023-02020-9

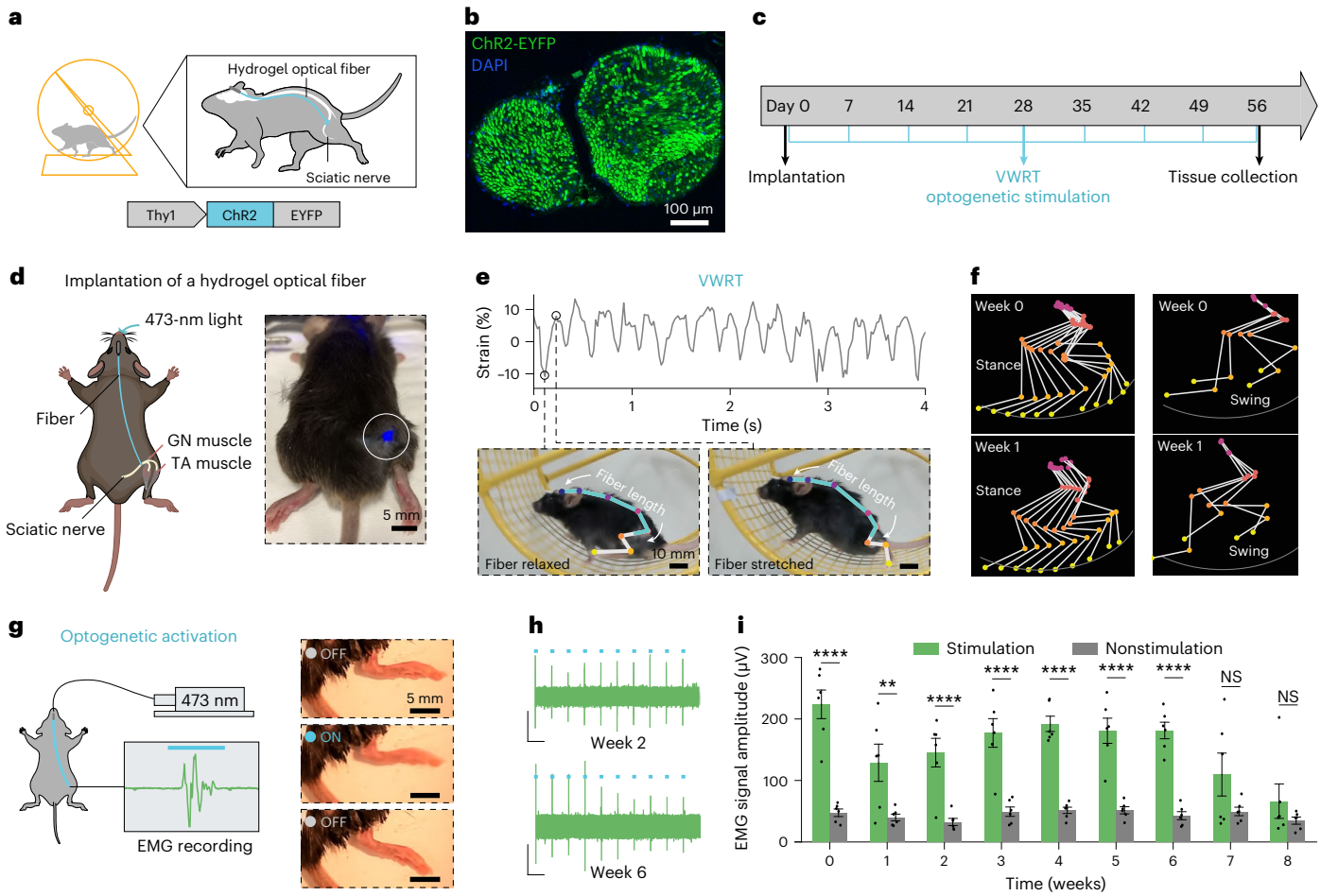


Fig. 3 | Optogenetic stimulation enabled by hydrogel optical fibers. a, Schematic showing the optogenetic stimulation of hindlimb muscles with a hydrogel fiber in Thy1::ChR2-EYFP transgenic mice. **b**, Confocal image of sciatic nerve cross-section showing ChR2-EYFP expression. Scale bar, 100 μm. **c**, In vivo study design and timeline of implantation, VWRT, optogenetic stimulation and tissue collection over 8 weeks. **d**, Schematic and image showing a mouse implanted with a hydrogel optical fiber. Scale bar, 5 mm. **e**, Representative plot of the mechanical strain of the hydrogel fiber in a mouse over time during VWRT. The bottom images show the pose estimation of a mouse implanted with a hydrogel fiber on a running wheel. The mouse is labeled with nodes for the ferrule, neck, back, iliac crest, hip, knee, ankle and toe. The fiber length, highlighted in blue, is calculated by the total length of the segments starting from the ferrule to the middle point between the hip and knee. Scale bars, 10 mm. **f**, Kinematic stick diagram of mouse hindlimb movement on a running wheel on week 0 before and week 1 after implantation. A gait cycle is composed of a stance phase (left) and a swing phase (right) in the stick diagram. The nodes represent the iliac crest, hip, knee, ankle and toe from top to bottom. **g**, Schematic showing the optogenetic stimulation controlled by optical pulses from a 473-nm light source and recorded by EMG. The left images show the ankle joint movement in response to optogenetic stimulation. Scale bars, 5 mm. **h**, Plots of EMG signals recorded on week 2 and week 6 after implantation. Blue bars indicate optical pulses with a pulse width of 10 ms and irradiance of 35.4 mW mm^{-2}. Scale bars, 1 s (x axis), 100 μV (y axis). **i**, Plot of EMG signal amplitude from week 0 before implantation to week 8 after implantation with and without optogenetic stimulation. One-way repeated measures ANOVA with Sidak's multiple comparison test for stimulation versus nonstimulation. **0.001 ≤ P ≤ 0.01; ****P ≤ 0.0001. GN, gastrocnemius; NS, not significant; TA, tibialis anterior.

deformation. Unlike silica fibers that constrained artery displacement, the hydrogel fibers followed tissue deformation and maintained stable light transmission under dynamic loading (Fig. 2j,k and Supplementary Video 2). To expand their versatility, we designed fiber distal ends with different architectures, including a hydrogel cuff interfacing with tubular organs (for example, peripheral nerves; Extended Data Fig. 4j) and a conformal hydrogel membrane tailored to organs with smaller curvatures (for example, heart; Extended Data Fig. 4k).

Optogenetic stimulation after repeated fiber deformation

To demonstrate in vivo light delivery with repeated deformation, we implanted the hydrogel fibers in mice with voluntary wheel running tests (VWRTs), a standard locomotor activity test (Fig. 3a). Transgenic Thy1::ChR2-EYFP mice, expressing excitatory opsin ChR2 in the nervous system (Fig. 3b), were implanted with fibers and then subjected to periodic VWRTs (n = 6 mice; Fig. 3c)[7,27]. During implantation, the hydrogel fiber's ferrule was affixed on the skull while the cuff was wrapped around the sciatic nerve (Fig. 3d). After implantation, the mice underwent 42-min weekly VWRTs during which the repeated stance and swing phases were accompanied by in vivo fiber cyclic stretching. To quantify the deformation of the implanted fibers, mouse running gait during VWRTs was analyzed with DeepLabCut markerless pose estimation (Fig. 3e,f and Supplementary Videos 3 and 4)[39]. By tracking the fiber length in pose estimation during running, we found that the fiber stretching frequency and the strain amplitude were approximately 4 Hz and 10%, respectively, indicating that the implanted hydrogel fibers experienced ~10,000 stretches per week with a strain amplitude of ~10% (Fig. 3e and Extended Data Fig. 5a–c). The fiber deformation amplitudes during grooming and rearing were found to be comparable to or below those associated with running (Extended Data Fig. 5d,e).

We then examined whether light delivered through the hydrogel fibers could activate the motor axons in Thy1::ChR2-EYFP mouse

https://doi.org/10.1038/s41592-023-02020-9

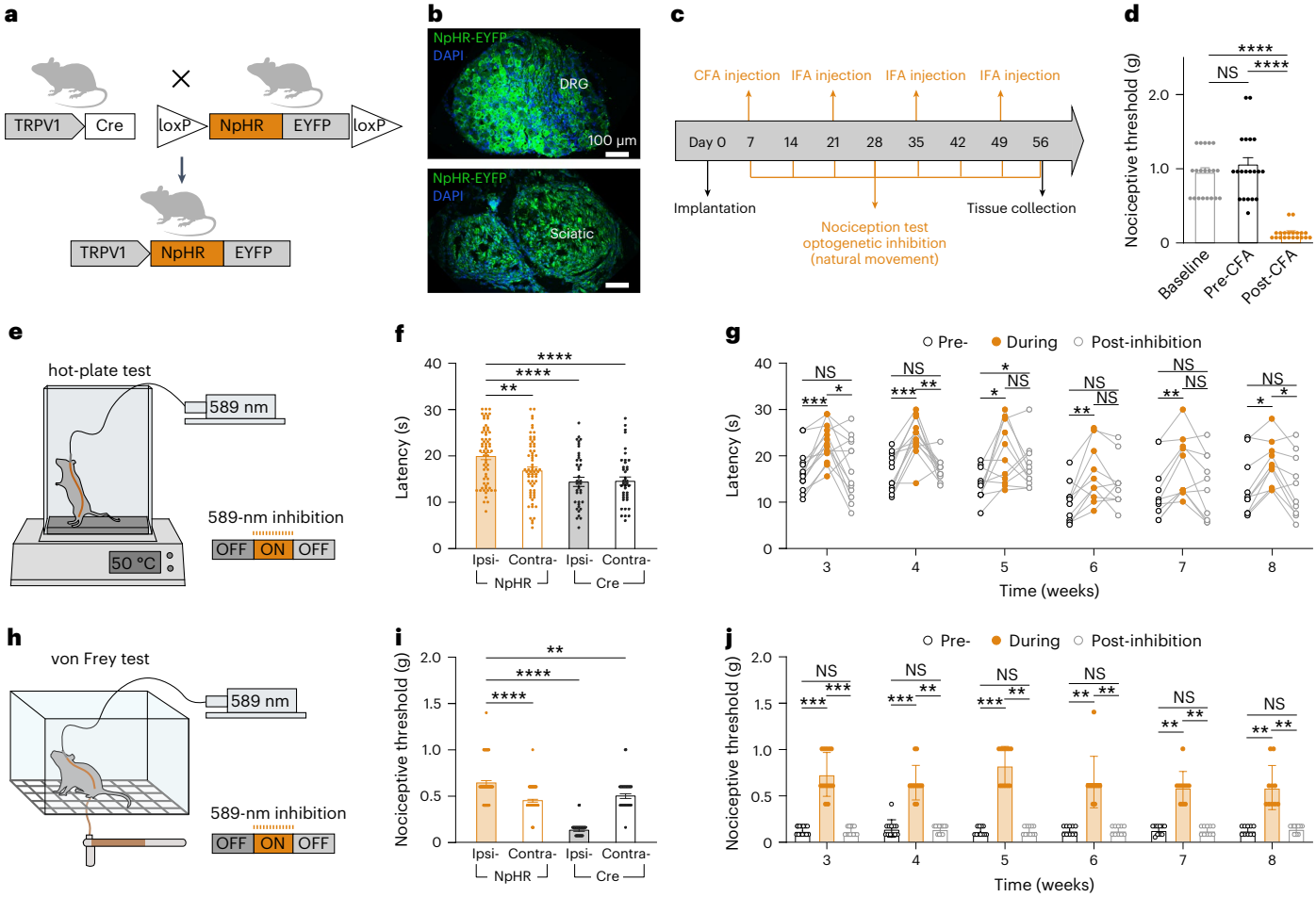


Fig. 4 | Optogenetic inhibition of nociception in naturally behaving mice enabled by hydrogel optical fibers. a, Schematic of the generation of TRPV1::NpHR-EYFP transgenic mice using a genetic cross approach. In these mice, inhibitory opsin is selectively expressed in the TRPV1-lineage of DRG sensory neurons. **b**, Confocal images of DRG and sciatic nerve cross-sections showing NpHR-EYFP expression. Scale bar, 100 μm. **c**, In vivo study design and timeline of implantation, inducing inflammatory pain with CFA and IFA injection, nociception test, optogenetic inhibition and tissue collection over 8 weeks. **d**, Nociceptive threshold of ipsilateral hind paw flinch before implantation (baseline), before CFA injection on day 6 post-implantation (pre-CFA) and after CFA on day 7 post-implantation (post-CFA) to confirm the CFA-induced inflammation through von Frey tests. **e**, Schematic showing a mouse with a hydrogel optical fiber in hot-plate tests. Optogenetic inhibition is controlled by optical pulses from a 589-nm laser source. Yellow bars indicate optical pulses with a pulse width of 25 ms and irradiance of 8.5 mW mm^{-2}. **f**, Latency of first-time ipsilateral and contralateral hind paw flinch during inhibition in evaluating thermal–nociceptive sensitivity through hot-plate tests for TRPV1::NpHR-EYFP (test group) and TRPV1::Cre (control group) mice from week 3 to week 8. **g**, Latency of first-time ipsilateral hind paw flinch in hot-plate tests for TRPV1::NpHR-EYFP mice over time after implantation. **h**, Schematic showing a mouse with a hydrogel optical fiber in von Frey tests. Optogenetic inhibition is controlled by optical pulses from a 589-nm light source. Yellow bars indicate optical pulses with a pulse width of 25 ms and irradiance of 8.5 mW mm^{-2}. **i**, Nociceptive threshold of ipsilateral and contralateral hind paw flinch during inhibition in evaluating mechanical allodynia through von Frey tests for TRPV1::NpHR-EYFP (test group) and TRPV1::Cre (control group) mice from week 3 to week 8. **j**, Nociceptive threshold of ipsilateral hind paw flinch in von Frey tests for TRPV1::NpHR-EYFP mice over time after implantation. *$0.01 \le P < 0.05$; **$0.001 \le P < 0.01$; ***$0.0001 \le P < 0.001$; ****$P < 0.0001$.

sciatic nerves. After VWRTs, we recorded the electromyographic (EMG) signals in mouse hindlimb muscles under anesthesia in response to the pulsed blue light (wavelength: 473 nm; estimated light intensity: 35.4 mW mm^{-2}; frequency: 1 Hz; ON: 10 ms; OFF: 990 ms). Optical stimuli consistently induced EMG signals in the tibialis anterior or gastrocnemius muscles (Fig. 3g and Extended Data Fig. 6a–c). Additionally, high-frequency optical pulses (40 Hz) resulted in tetanic muscle contractions (Extended Data Fig. 6d). In the long-term, optically evoked EMG potentials were recorded even 6 weeks after implantation (>60,000 fiber stretching cycles), indicating stable mechanical and optical properties of hydrogel fibers in vivo (Fig. 3h,i).

Effects of hydrogel fiber implantation on mice

To examine the potential effects of fiber implantation on locomotion, we first compared the running gait parameters during VWRTs, including stick diagrams, knee angles, ankle angles and gait frequency, before and after the implantation surgery. With the exception of a minor decrease in the maximum ankle angle in the first 2 weeks following surgery, we did not observe any considerable effects of fiber implantation on general locomotor performance (Fig. 3f and Extended Data Fig. 5f–o). The results from von Frey tests indicated the implantation procedure did not cause mechanical allodynia (Extended Data Fig. 7a–c). The skilled locomotor scores for the mouse hind paw on the implanted side temporarily decreased in horizontal ladder tests; however, the scores gradually returned to baseline levels during the recovery (Extended Data Fig. 7d–f). To examine the potential inflammation, we collected sciatic nerves after 8-week VWRTs and evaluated histology and immunohistochemistry. Histological evaluation showed that the implanted hydrogel cuffs did not cause severe foreign body reactions in the sciatic nerve at 8 weeks after implantation (Extended Data Fig. 7g,h).

Using ionized calcium-binding adapter molecule 1 (Iba1), a marker for macrophages in the peripheral nervous system[40,41], we also observed no notable increase in Iba1 expression in the implanted sciatic nerves compared with nonimplanted ones (Extended Data Fig. 7i–k; $P = 0.235$, unpaired t-test).

Furthermore, we examined possible adverse effects arising from optical illumination. Due to thermal dissipation within tissue, the photothermal effect in the sciatic nerves was found to be substantially smaller than that in air. At a coupled power of 45 mW, the temperature increase (ΔT) measured at the distal end of the hydrogel fiber was <0.4 °C, even at a 100% optical duty cycle (Extended Data Fig. 8a–f). Notably, due to the optimized refractive index contrast between the core and cladding and the light absorption in the cladding, the radial leakage and off-target illumination along the fiber were minimized, enabling targeted experiments in transgenic animals broadly expressing opsins across the central and peripheral nervous systems (Extended Data Fig. 8g–j). Additionally, we did not observe nerve dislocation due to fiber implantation and deformation during locomotion (Extended Data Fig. 8k–m), nor architectural change in the hydrogel cuff following 8-week implantation in mice (Extended Data Fig. 8n).

Optogenetic inhibition of nociception in behaving mice

We then evaluated the ability of the hydrogel optical fibers to modulate somatosensory neural pathways in behaving mice. To achieve this, we first created transgenic TRPV1::NpHR-EYFP mice, which expressed inhibitory rhodopsin NpHR fused with EYFP under the peptidergic nociceptor-specific promoter, transient receptor potential vanilloid receptor subtype 1 (TRPV1) (Fig. 4a)[29]. Confocal microscopy images confirmed NpHR-EYFP expression in the dorsal root ganglia (DRGs) and the sciatic nerves of TRPV1::NpHR-EYFP mice (Fig. 4b). To assess the efficacy of optogenetic inhibition in somatosensory afferents, we implanted hydrogel fibers in these mice and subjected them to sensory tests for up to 8 weeks. Chronic inflammatory pain was induced by intraplantar injection of complete Freund's adjuvant (CFA) 1 week following implantation, and maintained through biweekly incomplete Freund's adjuvant (IFA) injections (Fig. 4c). Consistent with earlier reports of the CFA inflammatory model, the mice developed mechanical allodynia (Fig. 4d)[42,43]. To evaluate the effects of optogenetic inhibition on thermal sensitivity, we placed the mice on a hot plate at 50 °C, and recorded the latency of their first-time hind paw flinch paired with yellow-light delivery to the sciatic nerves (wavelength: 589 nm; estimated light intensity: 8.5 mW mm^{-2}; frequency: 20 Hz; ON: 25 ms; OFF: 25 ms; 30-s duration) (Fig. 4e)[42,44]. At the same optical illumination conditions, the hind paw on the implanted side (ipsilateral, ipsi-) in NpHR-expressing mice exhibited substantially longer flinch latencies compared with the nonimplanted side (contralateral, contra-; $^{**}P = 0.0080$, Kruskal–Wallis analysis of variance (ANOVA) with Dunn's multiple comparison test) and the control group (TRPV1::Cre, $^{****}P < 0.0001$) implanted with identical fibers (Fig. 4f). Such diminished nocifensive behaviors upon light delivery were observed during the entire 8-week period (Fig. 4g and Extended Data Fig. 9a–e). Additionally, we employed von Frey tests to examine the effects of optogenetic silencing of TRPV1-expressing afferents on punctate mechanical allodynia, where normally innocuous tactile stimuli evoke pain (Fig. 4h)[42,44]. Consistent with the effects on thermal sensitivity, in TRPV1::NpHR-EYFP mice, yellow-light delivery through hydrogel fibers consistently attenuated mechanical allodynia over 8 weeks (Fig. 4i,j and Extended Data Fig. 9f–j), suggesting the utility of these fibers for studies of nociception in freely behaving mice.

Discussion

The hydrogel fiber technology offers a light delivery method for dynamic in vivo conditions, while preserving natural animal behaviors. By controlling the growth of polymeric nanocrystalline domains, we engineered fatigue-resistant hydrogel fibers with optimized mechanical and optical properties. This technology is compatible with fiber-coupled light sources and molecular optogenetic tools commonly found in neuroscience laboratories. Utilizing optogenetics in the peripheral nervous system, our method can be further leveraged to investigate motor control, somatosensation and pain processing[2,3,44]. Beyond the application in sciatic nerves, the hydrogel fibers can be tailored for implantation in peripheral nerves, as well as on other motile organs, such as the heart, gut and blood vessels[15,45,46]. We envision the capability and adaptability of our hydrogel fiber technology being expanded for bidirectional optogenetics stimulation and optical recording via the use of fluorescence indicators[13,47]. Such advances will facilitate future studies of peripheral neurophysiology in naturally behaving animals.

Online content

Any methods, additional references, Nature Portfolio reporting summaries, source data, extended data, supplementary information, acknowledgements, peer review information; details of author contributions and competing interests; and statements of data and code availability are available at https://doi.org/10.1038/s41592-023-02020-9.

References

1. Deisseroth, K. Optogenetics. *Nat. Methods* **8**, 26–29 (2011).
2. Kim, C. K., Adhikari, A. & Deisseroth, K. Integration of optogenetics with complementary methodologies in systems neuroscience. *Nat. Rev. Neurosci.* **18**, 222–235 (2017).
3. Montgomery, K. L., Iyer, S. M., Christensen, A. J., Deisseroth, K. & Delp, S. L. Beyond the brain: optogenetic control in the spinal cord and peripheral nervous system. *Sci. Transl. Med.* **8**, 337rv335–337rv335 (2016).
4. Nam, S. & Mooney, D. Polymeric tissue adhesives. *Chem. Rev.* **121**, 11336–11384 (2021).
5. Chen, R., Canales, A. & Anikeeva, P. Neural recording and modulation technologies. *Nat. Rev. Mater.* **2**, 1–16 (2017).
6. Liu, X., Liu, J., Lin, S. & Zhao, X. Hydrogel machines. *Mater. Today* **36**, 102–124 (2020).
7. Park, S. I. et al. Soft, stretchable, fully implantable miniaturized optoelectronic systems for wireless optogenetics. *Nat. Biotechnol.* **33**, 1280–1286 (2015).
8. Kathe, C. et al. Wireless closed-loop optogenetics across the entire dorsoventral spinal cord in mice. *Nat. Biotechnol.* **40**, 198–208 (2021).
9. Michoud, F. et al. Epineural optogenetic activation of nociceptors initiates and amplifies inflammation. *Nat. Biotechnol.* **39**, 179–185 (2021).
10. Zhang, Y. et al. Battery-free, fully implantable optofluidic cuff system for wireless optogenetic and pharmacological neuromodulation of peripheral nerves. *Sci. Adv.* **5**, eaaw5296 (2019).
11. Brooks, S. P. & Dunnett, S. B. Tests to assess motor phenotype in mice: a user's guide. *Nat. Rev. Neurosci.* **10**, 519–529 (2009).
12. Canales, A. et al. Multifunctional fibers for simultaneous optical, electrical and chemical interrogation of neural circuits in vivo. *Nat. Biotechnol.* **33**, 277–284 (2015).
13. Park, S. et al. Adaptive and multifunctional hydrogel hybrid probes for long-term sensing and modulation of neural activity. *Nat. Commun.* **12**, 3435 (2021).
14. Lu, C. et al. Flexible and stretchable nanowire-coated fibers for optoelectronic probing of spinal cord circuits. *Sci. Adv.* **3**, e1600955 (2017).
15. Buchanan, K. L. et al. The preference for sugar over sweetener depends on a gut sensor cell. *Nat. Neurosci.* **25**, 191–200 (2022).
16. Sparta, D. R. et al. Construction of implantable optical fibers for long-term optogenetic manipulation of neural circuits. *Nat. Protoc.* **7**, 12–23 (2012).
17. Liu, Y. et al. Soft and elastic hydrogel-based microelectronics for localized low-voltage neuromodulation. *Nat. Biomed. Eng.* **3**, 58–68 (2019).

18. Tringides, C. M. et al. Viscoelastic surface electrode arrays to interface with viscoelastic tissues. *Nat. Nanotechnol.* **16**, 1019–1029 (2021).
19. Yuk, H., Wu, J. & Zhao, X. Hydrogel interfaces for merging humans and machines. *Nat. Rev. Mater.* **7**, 935–952 (2022).
20. Guo, J. et al. Highly stretchable, strain sensing hydrogel optical fibers. *Adv. Mater.* **28**, 10244–10249 (2016).
21. Choi, M. et al. Light-guiding hydrogels for cell-based sensing and optogenetic synthesis in vivo. *Nat. Photonics* **7**, 987–994 (2013).
22. Bai, R., Yang, J. & Suo, Z. Fatigue of hydrogels. *Eur. J. Mech. A Solids* **74**, 337–370 (2019).
23. Liu, J. et al. Fatigue-resistant adhesion of hydrogels. *Nat. Commun.* **11**, 1071 (2020).
24. Kashyap, S., Pratihar, S. K. & Behera, S. K. Strong and ductile graphene oxide reinforced PVA nanocomposites. *J. Alloys Compd.* **684**, 254–260 (2016).
25. Oster, G. The scattering of light and its applications to chemistry. *Chem. Rev.* **43**, 319–365 (1948).
26. Rinawati, M., Triastuti, J. & Pursetyo, K. T. Characterization of elasticity and hydration of composite hydrogel based on collagen-iota carrageenan as a corneal tissue engineering. *IOP Conf. Ser. Earth Environ. Sci.* **137**, 012042 (2018).
27. Zheng, H. et al. A shape-memory and spiral light-emitting device for precise multisite stimulation of nerve bundles. *Nat. Commun.* **10**, 2790 (2019).
28. Liske, H., Qian, X., Anikeeva, P., Deisseroth, K. & Delp, S. Optical control of neuronal excitation and inhibition using a single opsin protein, ChR2. *Sci. Rep.* **3**, 3110 (2013).
29. Iyer, S. M. et al. Virally mediated optogenetic excitation and inhibition of pain in freely moving nontransgenic mice. *Nat. Biotechnol.* **32**, 274–278 (2014).
30. Antunes, P., Domingues, F., Granada, M. & André, P. *Mechanical Properties of Optical Fibers* (INTECH Open Access Publisher, 2012).
31. Guimarães, C. F., Gasperini, L., Marques, A. P. & Reis, R. L. The stiffness of living tissues and its implications for tissue engineering. *Nat. Rev. Mater.* **5**, 351–370 (2020).
32. Kuthe, C. D., Uddanwadiker, R. V. & Ramteke, A. Experimental evaluation of fiber orientation based material properties of skeletal muscle in tension. *Mol. Cell. Biomech.* **11**, 113–128 (2014).
33. Zwirner, J., Ondruschka, B., Scholze, M. & Hammer, N. Passive load-deformation properties of human temporal muscle. *J. Biomech.* **106**, 109829 (2020).
34. Kuthe, C. D. & Uddanwadiker, R. V. Investigation of effect of fiber orientation on mechanical behavior of skeletal muscle. *J. Appl. Biomater. Funct. Mater.* **14**, 154–162 (2016).
35. Layton, B. & Sastry, A. A mechanical model for collagen fibril load sharing in peripheral nerve of diabetic and nondiabetic rats. *J. Biomech. Eng.* **126**, 803–814 (2004).
36. Wang, Z. et al. Stretchable materials of high toughness and low hysteresis. *Proc. Natl Acad. Sci. USA* **116**, 5967–5972 (2019).
37. Griffith, A. A. VI. The phenomena of rupture and flow in solids. *Philos. Trans. R. Soc. Lond. A* **221**, 163–198 (1921).
38. Park, S., Loke, G., Fink, Y. & Anikeeva, P. Flexible fiber-based optoelectronics for neural interfaces. *Chem. Soc. Rev.* **48**, 1826–1852 (2019).
39. Nath, T. et al. Using DeepLabCut for 3D markerless pose estimation across species and behaviors. *Nat. Protoc.* **14**, 2152–2176 (2019).
40. Chiu, I. M. et al. Activation of innate and humoral immunity in the peripheral nervous system of ALS transgenic mice. *Proc. Natl Acad. Sci. USA* **106**, 20960–20965 (2009).
41. Kalinski, A. L. et al. Analysis of the immune response to sciatic nerve injury identifies efferocytosis as a key mechanism of nerve debridement. *eLife* **9**, e60223 (2020).
42. Liu, Y. et al. Touch and tactile neuropathic pain sensitivity are set by corticospinal projections. *Nature* **561**, 547–550 (2018).
43. Boettger, M. K. et al. Differences in inflammatory pain in nNOS-, iNOS- and eNOS-deficient mice. *Eur. J. Pain* **11**, 810–818 (2007).
44. Basbaum, A. I., Bautista, D. M., Scherrer, G. & Julius, D. Cellular and molecular mechanisms of pain. *Cell* **139**, 267–284 (2009).
45. Hsueh, B. et al. Cardiogenic control of affective behavioural state. *Nature* **615**, 292–299 (2023).
46. Sahasrabudhe, A. et al. Multifunctional microelectronic fibers enable wireless modulation of gut and brain neural circuits. *Nat. Biotechnol.* https://doi.org/10.1038/s41587-023-01833-5 (2023).
47. Gunaydin, L. A. et al. Natural neural projection dynamics underlying social behavior. *Cell* **157**, 1535–1551 (2014).

Publisher's note Springer Nature remains neutral with regard to jurisdictional claims in published maps and institutional affiliations.

Springer Nature or its licensor (e.g. a society or other partner) holds exclusive rights to this article under a publishing agreement with the author(s) or other rightsholder(s); author self-archiving of the accepted manuscript version of this article is solely governed by the terms of such publishing agreement and applicable law.

© The Author(s), under exclusive licence to Springer Nature America, Inc. 2023

Methods

Fabrication of short PVA-coated silica fibers

A short silica fiber (core diameter 400 µm, length 15 mm) was stripped from a multimode optical fiber (Thorlabs FT400UMT) and fixed to a ceramic optical ferrule (Thorlabs CFX440-10) using an epoxy adhesive (Loctite Eccobond F112). The silica fiber was extruded out at one end of the optical ferrule with the length of 3 mm, and both ends of the silica fiber in the optical ferrule were polished. The extruded silica fiber was treated with 50% sodium hydroxide solution overnight and plasma cleaning (Harrick Plasma) in an oxygen atmosphere for 5 min. A solution of 10 wt% PVA solution was prepared by dissolving 10 g of PVA (molecular weight of 146,000–186,000, 99+% hydrolyzed; Sigma-Aldrich) in 90 ml of water at 90 °C with continuous stirring for 5 h until clear. A layer of PVA was deposited on the extruded silica fiber surface by dip-coating in the 10 wt% PVA solution. After dip-coating, the optical ferrule with a short PVA-coated silica fiber was dried at room temperature for 1 h, heated at 100 °C for 1 h and rehydrated in water.

Fabrication of hydrogel optical fibers

A solution of 10 wt% PVA solution was prepared by dissolving 10 g of PVA (molecular weight of 146,000–186,000, 99+% hydrolyzed; Sigma-Aldrich) in 90 ml of water at 90 °C with continuous stirring for 5 h until clear. Next, two separate mixtures were prepared by mixing 10 ml of 10 wt% PVA solution with 75 µl of hydrochloric acid (37% in water) for 30 s using a planetary centrifugal mixer (Thinky AR-100), and 10 ml of 10 wt% PVA solution with 75 µl of glutaraldehyde solution (25% in water) for 30 s, respectively. These two solutions were then mixed for 30 s and degassed for 2 min. The resultant mixture was infused into a silicone tubing mold (length 120 mm, diameter 1.6 mm; McMaster-Carr 5233K51) connected to a disk-shaped acrylic mold (diameter 3 mm, thickness 6 mm; acrylic sheet by laser cutting) at the distal end. A PVA-coated optical ferrule was then inserted into the proximal end of the silicone tubing mold. The mixture in the mold was allowed to crosslink for 6 h at room temperature in a humid environment (relative humidity > 70%), after which the chemically crosslinked PVA hydrogel was demolded by swelling the silicone mold in DCM (Sigma-Aldrich). A hole (diameter 0.91 mm) was punched through in the center of the disk-shaped PVA hydrogel at the distal end using a dispensing tip (20 Gauge; EFD Nordson). The PVA hydrogel fiber was next washed in excess water to remove residual chemicals for 3 d, dried in air at room temperature for 12 h, annealed at 100 °C for 30 min and rehydrated in water to generate the hydrogel fiber without cladding. The processes of drying and annealing usually induce dimensional shrinkage of hydrogel fibers, so the fibers were kept straight during these processes to prevent nonuniform deformation. After being fully hydrated in water, each hydrogel fiber without cladding was inserted into silicone tubing (length 60 mm, diameter 1,000 µm; McMaster-Carr 1972T14) with both ends exposed. Then, 5 ml of 10 wt% PVA solution was mixed with 50 µl of hydrochloric acid (37%) for 30 s using a planetary centrifugal mixer (Thinky AR-100). Another 5 ml of 10 wt% PVA solution was mixed with 50 µl of glutaraldehyde solution (25% in water) for 30 s. The above two solutions as well as 5 ml of graphene oxide solution (6.2 g l^{-1} in water; Graphene Supermarket) were then mixed for 30 s and degassed for 2 min. The mixture was infused into the silicone tubing containing a hydrogel fiber without cladding and left for chemical crosslinking for 12 h, after which the hydrogel fiber with cladding was demolded by swelling the silicone mold in dichloromethane. To reduce the graphene oxide in the hydrogel cladding, the hydrogel fiber was incubated in 100 ml of aqueous solution containing 5 g of sodium hydroxide and 1.5 g of sodium hydrosulfite at 37 °C for 1 min to generate rGO. Lastly, the hydrogel fiber was washed with a large amount of water to remove residual chemicals for 2–3 d.

Optimization of hydrogel optical fibers

When fabricating short PVA-coated silica fibers, we varied the PVA amount (2.5–20.0 wt%) and the temperature (20–85 °C) of the dip-coating solution to control the thickness of the PVA-coating layer on the silica fibers (Supplementary Fig. 1a–d). When fabricating hydrogel core materials, we changed the glutaraldehyde amount (0.025–0.400 wt%) to regulate the chemical crosslinking density and the PVA annealing time (0–120 min) to regulate the crystallinity in the PVA hydrogel core materials (Extended Data Fig. 3d–i and Supplementary Fig. 2a–c). When fabricating hydrogel cladding materials, we varied the reduction time (0–5 min) to control the generation of rGO in the hydrogel cladding materials (Extended Data Fig. 3n–q). When fabricating different structures at the distal end of the hydrogel optical fibers, we designed different form factors of molds, including a disk-shape and a thin-film mold at the end of silicone tubing (Extended Data Fig. 4j,k).

Imaging of hydrogel optical fibers

We used an epifluorescence microscope (Nikon Eclipse LV100ND) with a ×5 objective lens to acquire microscopic images in the bright-field mode and to characterize the dimensional and structural features of hydrogel optical fibers. The images we obtained were used to identify the thickness of the PVA-coating layer on the silica fibers, the diameters of hydrogel optical fibers with and without cladding, the size of hydrogel cuffs and the hydrogel–silica adhesion before and after cyclic stretching. We used a digital single-lens reflex (DSLR) camera to capture the macroscopic images of hydrogel optical fibers in the dark-field mode. To facilitate visualization, light-absorbing cladding was not included in the experiments shown in Figs. 1l and 2g and Extended Data Fig. 3l,m. The two ends of the hydrogel optical fiber are connected to a light source and a photodetector, respectively, in Fig. 2g and Extended Data Fig. 3l,m.

Rheological measurement of PVA solutions

We utilized a rheometer (AR-G2, TA Instrument) equipped with a 40-mm 2° cone-plate and conducted the experiments in the steady-state flow mode to characterize the shear viscosity of PVA solutions. The measurements of the shear viscosity of the PVA solutions were carried out at different shear rates (0.01–100.00 s^{-1}), temperatures (20–85 °C) and PVA amounts (2.5–20.0 wt%). We identified the shear viscosity measured at a shear rate near zero.

X-ray scattering measurement of hydrogel core materials

The WAXS measurements were performed on the hydrogel core materials in the dry state using Ni-filtered CuKa1 radiation with an X-ray wavelength of 0.154 nm and a Pilatus3R 300K detector (Dectris) in a SAXSLAB instrument. We used a wide-angle 2-mm beamstop with a sample–detector distance of 109.1 mm. The exposure time was set as 300 s. Raw WAXS patterns were processed with corrections by MATLAB-based GIXSGUI software before analysis. After subtracting the instrumental line broadening, we identified the full-width at half-maximum diffraction peak as β, and the average size of nanocrystalline domains, d_{nd}, was approximately calculated using Scherrer's equation, $d_{nd} = k\lambda/(\beta \cos\theta_0)$, where k is a dimensionless shape factor varying with the actual shape of the nanocrystalline domain ($k = 1$, approximating the spherical shape of the nanocrystalline domains), λ is the wavelength of X-ray diffraction ($\lambda = 0.154$ nm) and θ_0 is the peak of the Bragg angle[39].

Differential scanning calorimetry of hydrogel core materials

We used a differential scanning calorimeter (Discovery, TA Instrument) to characterize the crystallinity of the hydrogel core materials in the dry state. The materials were placed in a Tzero Pan and heated from 50 °C to 250 °C at a rate of 20 °C min^{-1} under a nitrogen atmosphere with a flow rate of 30 ml min^{-1}. By tracking the heat flow curve ranging from 200 °C to 250 °C, we integrated the endothermic transition and obtained the enthalpy for melting the crystalline domains in the dry sample. The crystallinity can be calculated as H/H^0, where H is the measured melting enthalpy of hydrogel core materials, and $H^0 = 138.6$ J g^{-1} is the melting enthalpy of 100% crystalline PVA.

Absorbance measurement of hydrogel core and cladding materials

For absorbance measurement, hydrogel membranes were prepared with a similar procedure as discussed above but using a rectangular mold (thickness 1 mm). Final thicknesses of the hydrogel membranes were measured by a caliper. The light absorbances at 473 nm and 589 nm of the hydrogel materials were measured by a microplate reader (BioTek Synergy H4) in the unit of absorbance unit (AU) when they were immersed in PBS. We used the absorbance divided by thickness as the normalized absorbance (unit: AU mm^{-1}).

Transmittance spectrum measurement of hydrogel core and cladding materials

For transmittance spectrum measurement, hydrogel membranes were prepared with a similar procedure as discussed above but using a rectangular mold (thickness 1 mm). Final thicknesses were measured by a caliper. The transmission spectra (200–1,000 nm) of the hydrogel materials were measured by ultraviolet–visible spectroscopy (Thermo Fisher Scientific) when they were immersed in PBS.

Refractive index measurement of hydrogel core and cladding materials

For refractive index measurement, hydrogel membranes were prepared with a similar procedure as discussed above but using a rectangular mold (thickness 1 mm). The refractive indices of the hydrogel materials were measured by a digital pocket refractometer (Sper Scientific). After removing residual water on hydrated hydrogel membranes, we attached them onto the measuring prism surface of the refractometer. The Brix numbers shown on the refractometer were converted to refractive indices.

Ray tracing simulation in optical fibers

We performed ray tracing simulations in the optical fibers by using Ray Optics Simulation (https://phydemo.app/ray-optics/simulator/) to evaluate the effects of refractive index contrast between the hydrogel core and cladding. With the same configuration (core diameter 600 µm, cladding thickness 200 µm), we changed the refractive indices of hydrogel core materials from 1.40, to 1.36, to 1.34, and fixed the refractive index of hydrogel cladding materials as 1.34 and the refractive index of the environment as 1.33.

Attenuation measurement of hydrogel fibers

The intensity of transmitted light through hydrogel fibers of various lengths was measured using a power meter (Thorlabs PM16-122) when the fibers were kept in a simulated tissue medium (1 wt% agarose gel). First, the hydrogel fiber was inserted into a plastic tube (diameter 3 mm). Then, we injected 1 wt% agarose solution at 50 °C into the tube and allowed it to cool. Next, a light source (maximum power 200 mW, wavelength 473 nm; Changchun New Industries) was coupled into a hydrogel fiber. We measured the light intensity at the fiber terminal after cutting a 5-mm-long segment repeatedly. The attenuation coefficients α of the hydrogel fibers were obtained by fitting the experimentally measured light intensity to the equation: $-10\log_{10}(P/P_0) = \alpha L + \text{const}$, where P is the light intensity at any fiber length L, P_0 is the light intensity when the fiber length is zero and const is a constant value.

Light transmission measurement under deformation

The light transmission through optical fibers made of silica, PDMS and hydrogels was measured by a power meter (Thorlabs PM16-122), when the fibers were immersed in PBS. We used optic ferrules at both ends of the hydrogel fibers in the fabrication. We also connected both ends of PDMS fibers (Dow Corning Sylgard 184) with optic ferrules using glass–PDMS plasma bonding, and both ends of silica fibers (Thorlabs FT400UMT) with optic ferrules using epoxy adhesives (Loctite Eccobond F112). Then, one ferrule end of the fibers was coupled with a light source at 473 nm (maximum power 200 mW; Changchun New Industries), and another ferrule end was connected to a power meter to continuously measure the light intensity through optical fibers. During measurement, the fibers were immersed in PBS, and they were deformed using either a horizontal testing machine (CellScale) to stretch at different tensile strains or cylindrical disks to bend 360° with different bending radii. The measurements of light transmission were conducted on 3–4 independent samples.

Single-cycle tensile testing of hydrogel optical fibers

We performed single-cycle tensile tests on the hydrogel optical fibers when they were immersed in water at 25 °C using a horizontal testing machine (CellScale). The load cells with a maximum force of 4.4 N or 44 N were used. In single-cycle tensile tests, the hydrogel optical fibers (including an optic ferrule, a hydrogel core and a hydrogel cladding, gauge length 10 mm, core diameter 600 µm, cladding thickness 200 µm) were stretched until fractured by the testing machine at a strain rate of 5 mm s^{-1}. We recorded the force–displacement curves during tests to obtain the stress–strain curves. The nominal stress was calculated by dividing the force by the cross-sectional area of hydrogel optical fibers, and the strain was measured by dividing the displacement by the gauge length. We derived several parameters from the stress–strain curves, including Young's modulus, tensile strength, maximum strain and strain energy density.

Multiple-cycle tensile testing of hydrogel optical fibers

We performed multiple-cycle tensile tests using a horizontal testing machine (CellScale) on hydrogel optical fibers when they were immersed in water at 25 °C. The load cells with a maximum force of 4.4 N or 44 N were used. The hydrogel optical fibers (including an optic ferrule, a hydrogel core and a hydrogel cladding, gauge length 10 mm, core diameter 600 µm, cladding thickness 200 µm) were cyclically stretched by the testing machine at the frequency of 1 Hz in the strain-controlled or stress-controlled modes. In the strain-controlled mode of multiple-cycle tensile tests, the hydrogel optical fibers were stretched with a constant strain amplitude, and the stress variation was recorded over time. In the stress-controlled mode of multiple-cycle tensile tests, the hydrogel optical fibers were stretched with a constant stress amplitude, and the strain variation was recorded over time. The nominal stress was calculated by dividing the force by the cross-sectional area of hydrogel optical fibers, and the strain was measured by dividing the displacement by the gauge length. To obtain the stress–life curve (S–N curve) for fatigue analysis, we performed the multiple-cycle tensile tests in the stress-controlled mode and recorded the number of stretch cycles to failure for different stress amplitudes. We derived several parameters from the stress–life curves, including fatigue strength at multiple cycles.

Fatigue threshold measurement of hydrogel core materials

The fatigue threshold of hydrogel core materials was measured by performing a multiple-cycle tensile test on hydrogel membranes when they were immersed in water at 25 °C. We used a horizontal testing machine (CellScale) and load cells with a maximum force of 4.4 N and 44 N. The dumbbell-shaped notched hydrogel membrane made of core materials (width 5 mm, thickness 0.8 mm, gauge length 10 mm and initial crack length 1 mm) was cyclically stretched by the testing machine at the strain rate of 2 mm s^{-1} in the strain-controlled mode, during which the hydrogel membranes were immersed in water. In the strain-controlled mode of multiple-cycle tensile tests, the hydrogel optical fibers were stretched with a constant strain amplitude, and the crack extension was recorded as a function of cycle number. The applied energy release rate was calculated as $G = 2kcW$, where k is a slowing varying function of the strain amplitude λ as $k = 3\lambda^{-0.5}$, c is the current crack length at undeformed state and W is the strain energy

density measured in the unnotched sample as $W = \int_1^\lambda S\, d\lambda$. The interfacial crack propagation rate is dc/dN, where N is the cycle number. To obtain the plot of dc/dN versus G for fatigue analysis, we performed multiple-cycle tensile tests at varied strain amplitudes, and the fatigue threshold can be estimated by linearly extrapolating the plot of dc/dN versus G to the x intercept.

Fabrication of hydrogel adhesion on a silica substrate

We fabricated a PVA hydrogel membrane adhered to a silica substrate using similar chemistry to that described above. Specifically, a silica substrate was treated with 50% sodium hydroxide solution overnight and plasma cleaning (Harrick Plasma) in an oxygen atmosphere for 5 min. A layer of PVA was deposited on the silica substrate by spin-coating of the 10 wt% PVA solution. After coating, the silica substrate was dried at room temperature for 1 h, heated at 100 °C for 1 h and rehydrated in water. Then, a PVA hydrogel membrane was generated on the PVA-coated silica substrate following similar procedures, including chemical crosslinking by glutaraldehyde and hydrochloric acid in a rectangular acrylic mold, washing in water, drying in air at 25 °C, annealing at 100 °C and rehydrating in water.

Interfacial fatigue threshold measurement of the silica–hydrogel adhesion

The interfacial fatigue threshold of silica–hydrogel was measured by performing a multiple-cycle 90° peeling test. A nylon film (thickness 100 μm) was adopted as a stiff backing for the hydrogel membrane and bonded to its top surface using cyanoacrylate adhesives (Loctite 460). We used the multiple-cycle 90° peeling test (ASTM D2861) with a mechanical testing machine (2-kN load cell; Zwick/Roell Z2.5) and 90° peeling fixture (TestResources, G50). The hydrogel membranes on the silica substrates were cyclically peeled by the testing machine at the strain rate of 2 mm s^{-1} in the force-controlled mode, during which the hydrogel membranes were immersed in water. In the force-controlled mode of cyclic peeling tests, the hydrogel membranes were peeled and released repeatedly with a constant force amplitude, and the maximum displacement variation was recorded as the interfacial crack extension as a function of cycle number. The applied energy release rate was calculated as $G = F_a/W$, where F_a is the applied force amplitude and W is the width of hydrogel membrane, and the interfacial crack propagation rate as dc/dN, where c is the maximum displacement and N is the cycle number. To obtain the plot of dc/dN versus G for fatigue analysis, we performed the peeling tests at varied applied force amplitudes, and the interfacial fatigue threshold was estimated by linearly extrapolating the plot of dc/dN versus G to the x intercept.

Interfacing porcine arteries with hydrogel optical fibers

We demonstrated tissue–fiber interactions by interfacing porcine arteries with optical fibers made of silica and hydrogels. Porcine arteries (length 15 mm) were purchased from a commercial vendor of research-grade porcine tissues (Sierra for Medical Science). The silica and hydrogel optical fibers were fixed to the artery surfaces using cyanoacrylate adhesives (Loctite 460). The arteries were then connected to a dispensing system (Nordson EFD), which pumped airflow to the artery repeatedly at the frequency of 1 Hz.

Mice

All animal procedures followed animal care guidelines which had been reviewed and approved by the Committee on Animal Care at Massachusetts Institute of Technology (MIT) and the Institutional Animal Care and Use Committee at the University of Massachusetts Amherst (UMass Amherst). Investigators were not blinded to the genotypes of the mice. Thy1::ChR2-EYFP (JAX 007612), TRPV1::Cre (JAX 017769) and RCL-eNpHR3.0/EYFP (Ai39, JAX 014539) mice were purchased from the Jackson Laboratory, and bred by the Division of Comparative Medicine at MIT and the Animal Care Service at UMass Amherst. The TRPV1::Cre mouse line expresses Cre recombinase under the control of the TRPV1 promoter, ensuring specific targeting of TRPV1-expressing cells. The RCL-eNpHR3.0/EYFP mouse line carries a Cre-dependent reporter construct with an enhanced halorhodopsin (eNpHR3.0). The breeding of TRPV1::NpHR-EYFP mice was carried out by crossing male homozygous TRPV1::Cre mice with female homozygous RCL-eNpHR3.0/EYFP mice. Genotyping of offspring was performed using PCR analysis of ear snip DNA samples to confirm the presence of both TRPV1::Cre and RCL-eNpHR3.0/EYFP alleles. All mice were housed in plastic cages with disposable bedding on a standard light cycle (lights on at 07:00 and off at 19:00) with food and water available ad libitum. More detailed mouse information is provided in Supplementary Table 1.

In vivo implantation of hydrogel optical fibers

Mice were anesthetized with 1.5–2.0% isoflurane in oxygen, and their body temperature was maintained using a heated surgical table. Before surgical procedures, the skin areas on the hindlimb and head were cleaned with a depilatory agent (Nair Hair Remover Lotion) followed by povidone-iodine and ethanol scrub. Under sterile conditions, skin incisions were made on the head to expose the skull and on the hindlimb to expose the mid-thigh muscle. The vastus lateralis muscle and biceps femoris muscle were then bluntly separated to access the sciatic nerve. Next, a hydrogel fiber was threaded subcutaneously from the hindlimb incision to the head incision using a spatula. Then, the hydrogel cuff at the distal end of the hydrogel fiber was placed around the sciatic nerve. The cut on the hydrogel cuff was sealed with a tissue adhesive (B. Braun Histoacryl), and the skin incision on the hindlimb was then sutured back with Nylon 5-0 suture (Ethicon). Finally, the optical ferrule at the proximal end of the hydrogel fiber was affixed to the skull at a 10–20° angle to the horizontal with two self-curing dental cements (C&B Metabond Quick Cement System and Lang Jet Set-4). Thy1::ChR2-EYFP ($n = 15$), TRPV1::NpHR-EYFP ($n = 13$) and TRPV1::Cre ($n = 7$) mice were implanted with hydrogel fibers.

VWRTs

Mice were placed on a wire mesh running wheel (diameter 20 cm; Prevue Pet Products) in an acrylic chamber to allow voluntary running before and after implantation. At 1 d before surgery, the animals were habituated to the wheel for 42 min. Starting 1 week following fiber implantation, mice underwent 42-min VWRTs weekly. Thy1::ChR2-EYFP mice ($n = 6$) with implanted hydrogel fibers were subjected to VWRTs during weeks 0–8 following surgery.

Gait analysis of mouse behaviors

We recorded the animal natural behaviors during running, grooming and rearing using a camera (Logitech Brio Ultra Pro HD Webcam). Then, we performed kinematic analysis on the recorded animal natural behaviors using a markerless pose estimation software (DeepLabcut)[39]. We labeled and tracked a few mouse body parts including ferrule, neck, back, iliac crest, hip, knee, ankle and toes during animal behaviors. Using a custom algorithm written in MATLAB, a single gait cycle in VWRTs was determined between two local minimums in the plot of distance between the fore toe and hind toe over time, and divided into the swing phase and stance phase during VWRTs. The kinematic stick diagrams of hindlimb movement for a single gait cycle were extracted. The time-dependent fiber length was calculated from the total length of the segments between the ferrule and the middle point of the hip and knee. The initial fiber length was measured before the implantation surgery. From the time-lapse gait information, we obtained the variation of the knee angle and ankle angle, frequency of running gait and fiber stretching, and fiber strain.

Optogenetic stimulation in mice

We performed the optogenetic muscle stimulation experiments in Thy1::ChR2-EYFP mice during (week 0) and post (from week 1 to week

8) fiber implantation. Before the experiments, the mice finished their weekly VWRTs. The experiments were performed when the mice were anesthetized with 1% isoflurane, and body temperature was maintained with a heated surgical table. For optical stimulus, a laser (wavelength 473 nm; Changchun New Industries) was connected to the optical ferrule on the mouse skull. Pulsed stimulation of 10-ms pulse width and 1-Hz frequency was applied (ON: 10 ms; OFF: 990 ms; 1% duty cycle) and delivered to the sciatic nerve through the implanted hydrogel fiber. By placing a power meter (Thorlabs PM16-122) at the distal end of the hydrogel fiber, we measured the in vitro light intensity to be 35.4 mW mm^{-1} and estimated the in vivo light intensity to be the same. For EMG recordings, an electrode was inserted into the ipsilateral gastrocnemius muscle, and a reference electrode was subcutaneously inserted into the contralateral gastrocnemius muscle. The pair of electrodes (Ultra Disposable Subdermal Needle Electrodes, Natus Medical) were attached to a PZ2-32 amplifier connected to an RZ5D base processor (Tucker-Davis Technologies). We also changed stimulation parameters, including another frequency of optical pulses at 40 Hz, another light intensity at 145 mW mm^{-1} and another position of the detection electrode in the tibialis anterior muscle. Thy1::ChR2-EYFP mice (n = 6) with implanted hydrogel fibers were subjected to optogenetic stimulation during weeks 0–8 following surgery.

Evaluation of skilled locomotion using horizontal ladder tests

Mice were trained to walk on a horizonal ladder containing 80 metal rungs (diameter 3 mm, width 50 mm, spacing 10 mm). We used a camera (GoPro HERO8 Camera) to record the mouse walking behavior on the horizontal ladder. A score of 0–2 was given for each step for the ipsilateral hind paw. A score of 2 indicated normal walking behavior with successful grasping, a score of 1 indicated a slight slip followed by quick adjustment to regain balance and a score of 0 indicated a complete loss of balance resulting in a fall. To increase the accuracy, we calculated the average score for each mouse by dividing the total scores achieved on the horizontal ladder by the total number of steps taken. Thy1::ChR2-EYFP mice (n = 9) with implanted hydrogel optical fibers were subjected to horizontal ladder tests during weeks 0–8 following surgery.

Temperature measurement in hydrogel cuffs

The temperature measurements were carried out at the distal end of the hydrogel optical fiber, when hydrogel optical fibers were either in air or implanted in mice. To achieve this, we inserted a microscale resistance temperature detector at the hydrogel cuff when the fiber was connected to a light source (wavelength: 473 nm; estimated light intensity: 35.4 mW mm^{-2}; duty cycle: 1%, 10%, 25% or 100%).

Evaluation of off-target illumination and sciatic nerve dislocation

When hydrogel optical fibers with and without cladding were implanted in mice and connected to a light source, we identified the effects of off-target illumination along the fibers when the light source was on. We set up visualization tools, including labels on the skin and bare hydrogel optical fibers without cladding implanted, when the animals were anesthetized. The skin on top of the sciatic nerve was labeled with a green sticker to identify the original sciatic nerve position. Contours of the hydrogel optical fiber without cladding were visible in the dark-field, and the fiber terminal indicated the current sciatic nerve position. We tracked the relative displacement of the sciatic nerve at different states.

Induction and maintenance of inflammatory pain

Before evaluation of mechanical and thermal sensitivity in TRPV1::NpHR-EYFP and TRPV1::Cre mice, inflammatory pain was induced through intraplantar injection of CFA (Sigma-Aldrich F5881) or IFA (Sigma-Aldrich F5506). CFA or IFA suspension was first diluted with an equal volume of 0.9% sodium chloride solution. Then, 10 µl of diluted CFA or IFA suspension was injected subcutaneously into the hind paw to generate localized inflammatory pain. TRPV1::NpHR-EYFP (n = 13) and TRPV1::Cre (n = 7) mice with implanted hydrogel fibers were subjected to CFA and IFA injections.

Evaluation of mechanical sensitivity using von Frey tests

Mice were individually placed into a transparent acrylic chamber (length 7 cm, height 10 cm) with a metal mesh floor elevated 30 cm above a table. After a 30-min habituation period, a series of eight calibrated von Frey monofilaments (bending force 0.04 g, 0.07 g, 0.16 g, 0.40 g, 0.60 g, 1.00 g, 1.40 g, 2.00 g; Bioseb) were applied to the plantar surface of the ipsilateral (implanted) or contralateral (nonimplanted) hind paw for approximately 1 s, with a 30-s interval between each stimulus. Each monofilament was applied ten times, and the number of immediate hind paw flinches to each force was recorded. The force at which the paw flinch occurred at least six times was considered the nociceptive threshold. Thy1::ChR2-EYFP (n = 9) mice with implanted hydrogel fibers were subjected to von Frey tests during weeks 0–4 following surgery, and TRPV1::NpHR-EYFP (n = 13) and TRPV1::Cre (n = 7) mice with implanted hydrogel fibers were subjected to von Frey tests during weeks 0–8 following surgery. All von Frey tests were performed in naturally moving mice.

Evaluation of thermal sensitivity using hot-plate tests

Mice were individually placed into a transparent acrylic chamber (diameter 19 cm, height 26 cm) on a heated metal surface (length 26.5 cm, width 26.5 cm) which was maintained at 50 ± 0.1 °C (Harvard Apparatus). Each hot-plate test lasted for ≤30 s, with a 30-min interval between each stimulus to prevent heat-related injury. The latency for a mouse to exhibit its first-time hind paw flinch was recorded, after which it was immediately removed from the hot-plate. TRPV1::NpHR-EYFP (n = 13) and TRPV1::Cre (n = 7) mice with implanted hydrogel fibers were subjected to hot-plate tests during weeks 0–8 following surgery. All hot-plate tests were performed in naturally moving mice.

Optogenetic inhibition of nociception in naturally behaving mice

We performed the experiments of optogenetic nociception inhibition in TRPV1::NpHR-EYFP and TRPV1::Cre mice from week 3 to week 8 post fiber implantation. During the experiments, the naturally behaving mice were subjected to von Frey and hot-plate tests. For optical stimulus, a laser (maximum power 300 mW, wavelength 589 nm; Ningbo Yuanming Laser Technology) was connected to the optical ferrule on the mouse skull. Pulsed stimulation of 25-ms pulse width and 20-Hz frequency was applied (ON: 25 ms; OFF: 25 ms; 50% duty cycle) and delivered to the sciatic nerve through the implanted hydrogel fiber. By placing a power meter (Thorlabs PM16-122) at the distal end of the hydrogel fiber, we measured the in vitro light intensity to be 8.5 mW mm^{-1} and estimated the in vivo light intensity to be the same. Mice underwent thermal and mechanical sensitivity tests, during which the yellow-light pulses were delivered. TRPV1::NpHR-EYFP mice (week 3, n = 13; week 4, n = 12; week 5, n = 11; weeks 6–8, n = 10) in the test group and TRPV1::Cre mice (week 3–5, n = 7; weeks 6–8, n = 6) in the control group were subjected to optogenetic inhibition during weeks 0–8 following surgery.

Tissue collection

Once mice were euthanized, their sciatic nerves and DRGs were removed from the body, washed briefly in PBS and fixed in 4% paraformaldehyde for more than 48 h at 4 °C in the dark. For immunohistochemistry staining, fixed tissues were then placed in 30% sucrose in PBS overnight at 4 °C in the dark. Next, the tissues were embedded in Tissue-Tek OCT compound (Sakura Finetek 4583) and cut into 20-µm transverse sections using a cryostat microtome (Leica CM1950).

Immunohistochemistry staining to confirm transgenic expression

We performed immunohistochemistry staining for the transverse sections of TRPV1::NpHR-EYFP sciatic nerves to confirm the successful genetic crossing. A blocking solution containing 1 wt% BSA (Sigma-Aldrich A9647) and 0.5 v/v% Triton X-100 (Sigma-Aldrich X100) was used for antibody dilution, and first added to the sciatic nerve slices for 30 min. The chicken polyclonal antibodies (pAb) anti-GFP antibody (Abcam ab13970) as the primary antibody was diluted in the blocking solution at a ratio of 1:400, and incubated with the sciatic nerves overnight at 4 °C. Then, the goat anti-chicken IgY (H + L), Alexa Fluor 488 (Invitrogen A-11039), as the secondary antibody was diluted in the blocking solution at a ratio of 1:1,000, and incubated with the sciatic nerves for 2 h at room temperature. Meanwhile, the transverse sections of TRPV1::NpHR-EYFP DRGs and Thy1::ChR2-EYFP sciatic nerves did not require anti-GFP staining, and they were immersed in a blocking solution containing 0.5 v/v% Triton X-100 for 30 min. Next, the anti-GFP stained and nonstained sections were placed on microscopic slides (Superfrost Plus Microscope Slide) and mounted with a mounting medium containing DAPI (Fluoromount-G Mounting Medium with DAPI, Invitrogen). Finally, the slides were imaged under a confocal microscope (Leica TCS SP2) with a ×40 oil immersion objective lens.

Immunohistochemistry staining for immune response evaluation

We collected ipsilateral and contralateral sciatic nerves after 8-week experiments, and performed immunohistochemistry staining for transverse sections of sciatic nerves. A blocking solution containing 1 wt% BSA (Sigma-Aldrich A9647) and 0.5 v/v% Triton X-100 (Sigma-Aldrich X100) was used for antibody dilution and first incubated with the sciatic nerves for 30 min. The rabbit monoclonal antibodies (mAb) anti-Iba1 (Abclonal A19776) as the primary antibody was diluted in the blocking solution at a ratio of 1:200, and incubated with the sciatic nerves overnight at 4 °C. Then, the donkey anti-rabbit IgG (H + L), Alexa Fluor 568 (Invitrogen A-10042), as the secondary antibody was diluted in the blocking solution at a ratio of 1:1,000, and incubated with the sciatic nerves for 2 h at room temperature. Next, sections of sciatic nerves with anti-Iba1 staining were placed on microscopic slides (Superfrost Plus Microscope Slide) and mounted with a mounting medium containing DAPI (Fluoromount-G Mounting Medium with DAPI, Invitrogen). Finally, the slides were imaged under a confocal microscope (Leica TCS SP2) with a ×40 oil immersion objective lens.

Histology staining for immune response evaluation

Fixed tissue samples were placed into 70% ethanol and submitted for histological processing and hematoxylin and eosin staining in the Histology Facility at the Koch Institute for Integrative Cancer Research at MIT. Representative images of each group are shown in the corresponding figures.

Cost analysis of hydrogel optical fibers

Considering the price for raw materials in hydrogel optical fiber fabrication, we estimated the cost to be US$0.17 per fiber. This included the short silica fiber (US$0.04), PVA (US$0.005), glutaraldehyde (less than US$0.001), hydrochloric acid (less than US$0.001) and graphene oxide (US$0.12). Miscellaneous expenses (for example, optical ferrules for light source connection) and production costs (for example, labor and overheads) were not considered.

Statistical analysis

Statistical analyses were performed in GraphPad Prism 9 and OriginPro 2023. We first performed Shapiro–Wilks tests for data normality. For independent data with normal distribution, we used one-way ANOVA with Tukey's multiple comparison test. For independent data with non-normal distribution, we used Kruskal–Wallis ANOVA with Dunn's multiple comparison test. For paired data with normal distribution, we used one-way repeated measures ANOVA with Tukey's multiple comparison test. For paired data with non-normal distribution, we used Friedman tests with Dunn's multiple comparison test. *P* values less than 0.05 were considered significant: $*0.01 \le P < 0.05$, $**0.001 \le P < 0.01$, $***0.0001 \le P < 0.001$, $****P < 0.0001$. Detailed statistical information for the figures, Extended Data figures and Supplementary figures is included in Supplementary Tables 2–21.

Reporting summary

Further information on research design is available in the Nature Portfolio Reporting Summary linked to this article.

Data availability

The data associated with this study are available in the article and the Supplementary Information. Source data are provided with this paper. In addition, the original data for the material characterization, optogenetic stimulation, biocompatibility test, behavior test and pain inhibition have been deposited in the public repository figshare (https://figshare.com) and are accessible at https://doi.org/10.6084/m9.figshare.c.6703152.v3.

Code availability

The codes for EMG data extraction, running cycle counting and horizontal walk scoring used in this work are available at https://doi.org/10.6084/m9.figshare.c.6703152.v3 under an MIT license.

Acknowledgements

This work is supported in part by the National Institutes of Health (grant no. 1R01HL153857-01, grant no. 1R01HL167947-01, X.Z.), the National Science Foundation (grant no. EFMA-1935291, X.Z.), the US Army Research Office through the Institute for Soldier Nanotechnologies at MIT (grant no. W911NF-13-D-0001, X.Z.), Department of Defense Congressionally Directed Medical Research Programs (grant no. PR200524P1, X.Z.), the National Institutes of Health (grant no. K99-MH120279, grant no. R00-MH120279, S.R.), the Brain and Behavior Research Foundation (grant no. 29878, S.R.), UMass Amherst Faculty Research Grant (grant no. P1FRG0000000295, S.R.), the National Institute of Neurological Disorders and Stroke (grant no. R01-NS086804 and grant no. R01-NS115025, P.A.), the McGovern Institute for Brain Research (P.A.), the Hock E. Tan and K. Lisa Yang Center for Autism Research (P.A.) and the K. Lisa Yang Brain-Body Center (P.A.). A.S. was supported by the Lore Harp McGovern Fellowship.

Author contributions

These authors contributed equally: P.A., X.Z., X.L. and S.R. P.A. and X.Z. discussed the initial concept of the hydrogel optical fibers. X.L., S.R., S.L. and S.H. designed the materials and fabrication methods for the hydrogel optical fibers. X.L., J.N. and S.L. designed and conducted the characterization of materials and devices and data analysis. X.L., S.R., W.C., A.S., Q.W. and E.H. conducted the in vivo and ex vivo experiments and data analysis. X.L., S.R., K.F., W.C., J.X., Y.L., Z.H., J.X. and T.Y. designed the behavior assays and conducted the behavioral analysis. X.L., S.R., P.A. and X.Z. wrote the manuscript with input from all authors.

Competing interests

P.A. has a financial interest in NeuroBionics Inc., a biotechnology company focused on the development of multifunctional fibers for research and clinical applications. X.Z. has a financial interest in SanaHeal, a biotechnology company focused on the development of medical devices for surgical sealing and repair. Z.H. is an advisor for

Myro Therapeutics, Axonis and Rugen Therapeutics. The remaining authors declare no competing interests.

Additional information

Extended data is available for this paper at https://doi.org/10.1038/s41592-023-02020-9.

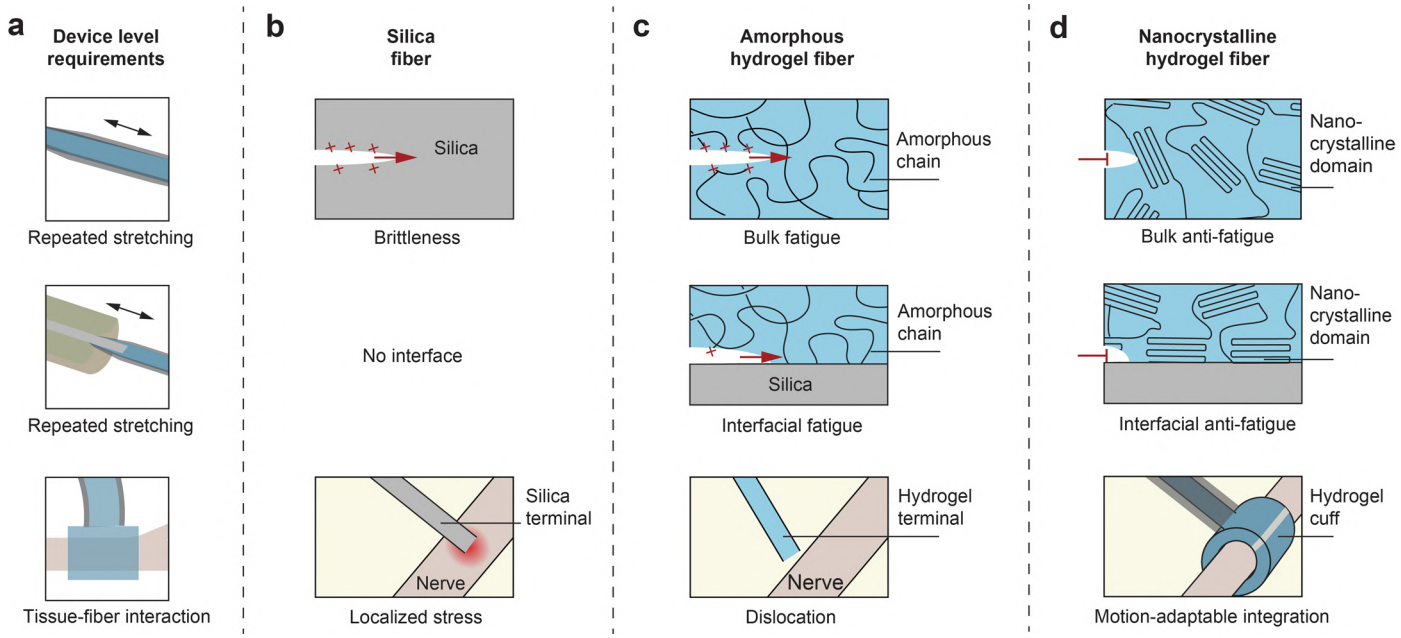
Supplementary information The online version contains supplementary material available at https://doi.org/10.1038/s41592-023-02020-9.

Correspondence and requests for materials should be addressed to Xinyue Liu, Siyuan Rao, Polina Anikeeva or Xuanhe Zhao.

Peer review information *Nature Methods* thanks the anonymous reviewers for their contribution to the peer review of this work. Primary Handling Editor: Nina Vogt, in collaboration with the *Nature Methods* team.

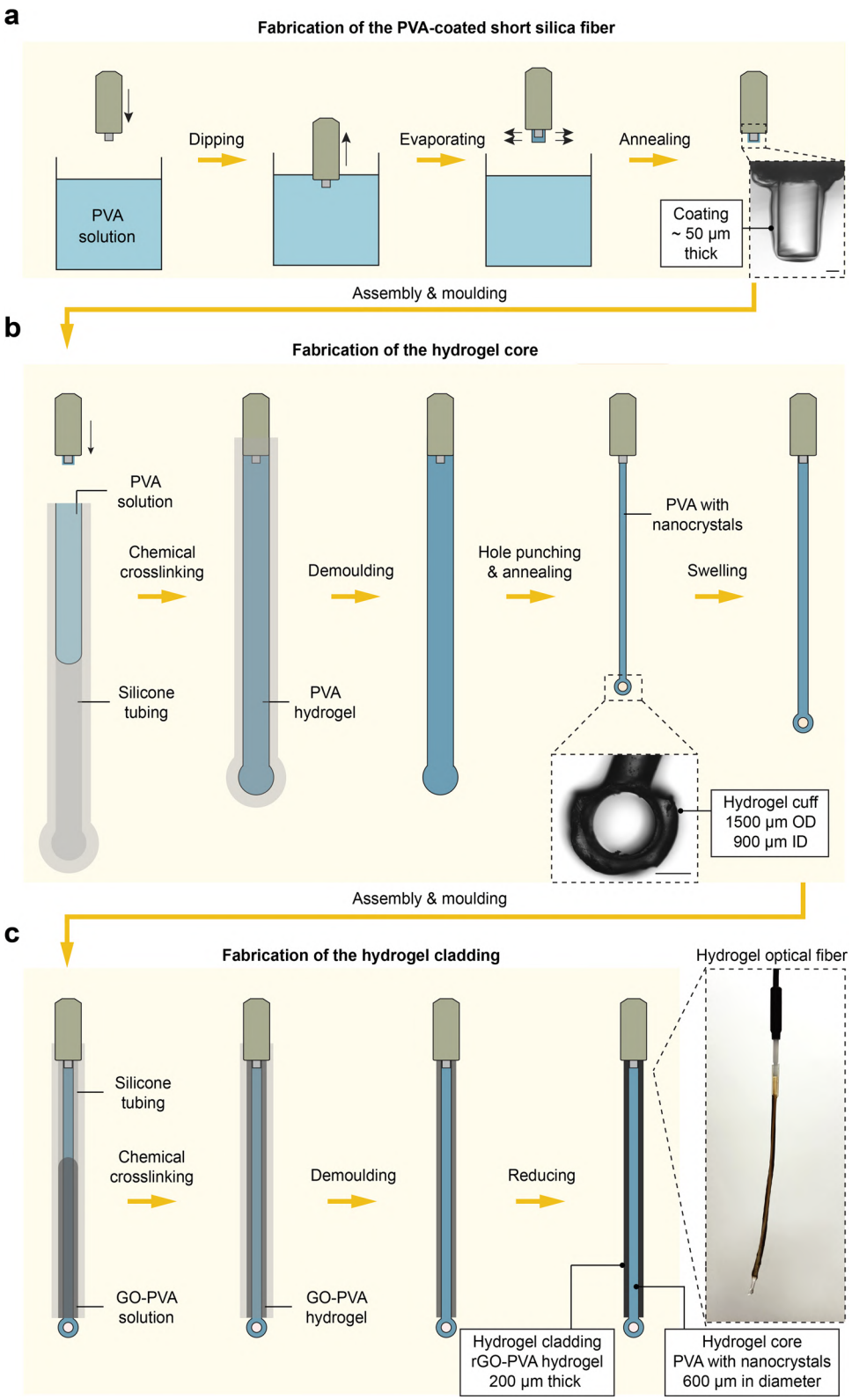
Reprints and permissions information is available at www.nature.com/reprints.

https://doi.org/10.1038/s41592-023-02020-9



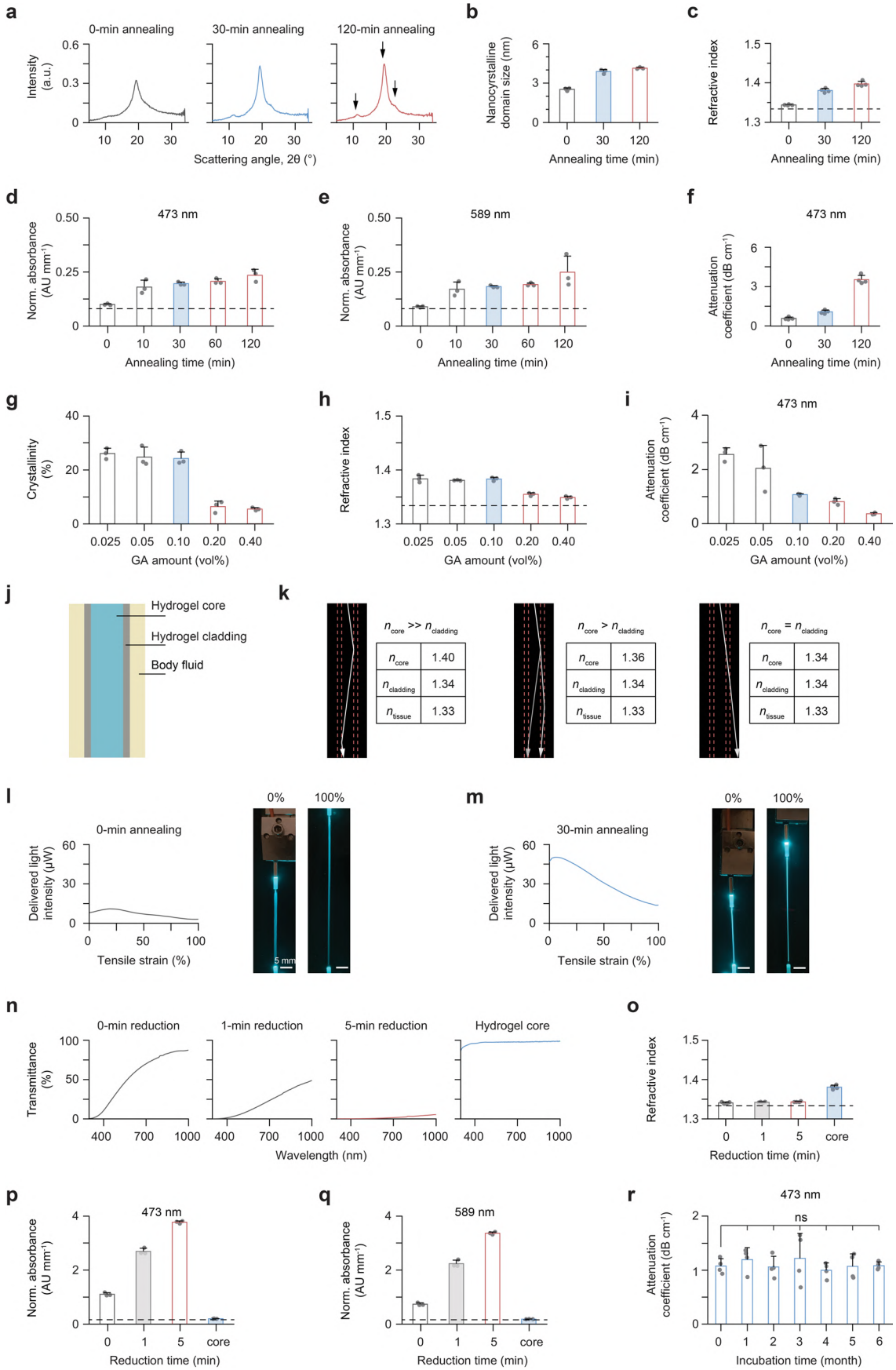
Extended Data Fig. 1 | Mechanical design principles for peripheral nerve optogenetics. a, Light delivery to peripheral nerves under persistent deformation faces challenges including repeated stretching of the bulk fiber and at the fiber-silica and the tissue-fiber interfaces. **b**, Using a silica fiber with high stiffness and high brittleness leads to fatigue failure under repeated stretching and localized mechanical stress at the silica fiber terminal. **c**, Using an amorphous hydrogel fiber with high compliance but high brittleness leads to fatigue failure under repeated stretching and no tissue integration at the hydrogel fiber terminal. **d**, Using a nanocrystalline hydrogel fiber with polymeric nanocrystalline domains leads to fatigue-resistance under repeated stretching and motion-adaptable integration between a hydrogel cuff and a target tissue.

https://doi.org/10.1038/s41592-023-02020-9



Extended Data Fig. 2 | Fabrication procedures of hydrogel optical fibers. a, Fabrication of polyvinyl alcohol (PVA)-coated short silica fibers. The silica fiber in a ceramic optic ferrule was dip-coated within a PVA solution, and then the PVA solution was allowed to dry and annealed to form the PVA hydrogel coating (50-μm-thick in the swollen state). **b**, Fabrication of hydrogel cores. The hydrogel core was fabricated by chemical crosslinking of the PVA solution in a silicone mold, together with the PVA-coated optic ferrule at one end and a disk-shaped compartment (3 mm in diameter) at the other end. The chemically crosslinked hydrogel core was then demolded, washed, dried, annealed, and swollen. By hole punching, the hydrogel cuff at the other end of the hydrogel core has the dimensions of 1500 μm in outer diameter and 900 μm in inner diameter in the dry state. **c**, Fabrication of hydrogel claddings. After inserting the hydrogel core into another silicone mold, the graphene oxide (GO)-PVA hydrogel was chemically crosslinked on the surface of the hydrogel core. After crosslinking and demolding, it was then reduced to reduced graphene oxide (rGO)-PVA hydrogel cladding. The resulting hydrogel core is 600 μm in diameter and the hydrogel cladding is 200 μm thick. The inset is an image of a hydrogel fiber connected to a light source.

https://doi.org/10.1038/s41592-023-02020-9

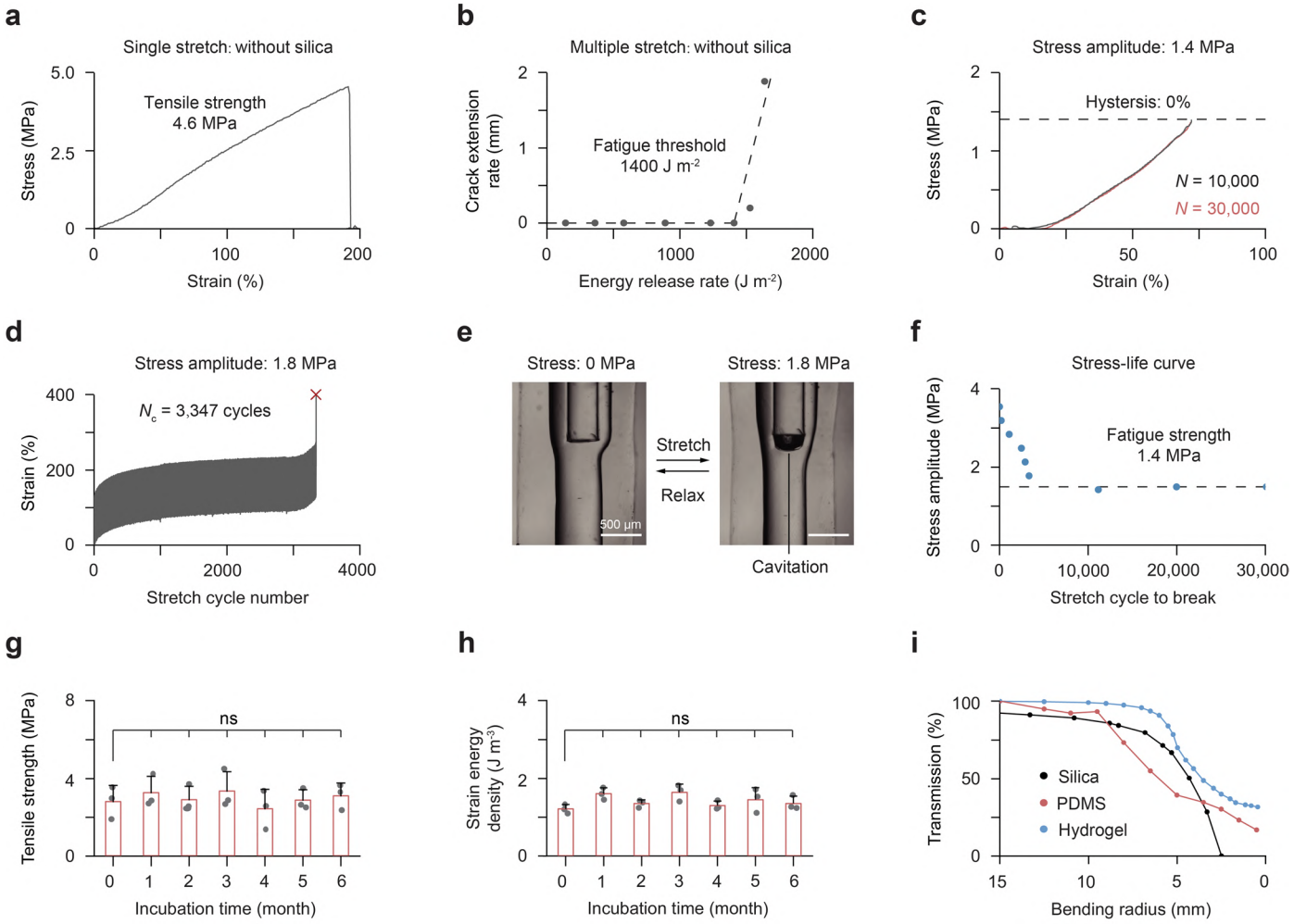


Extended Data Fig. 3 | See next page for caption.

https://doi.org/10.1038/s41592-023-02020-9

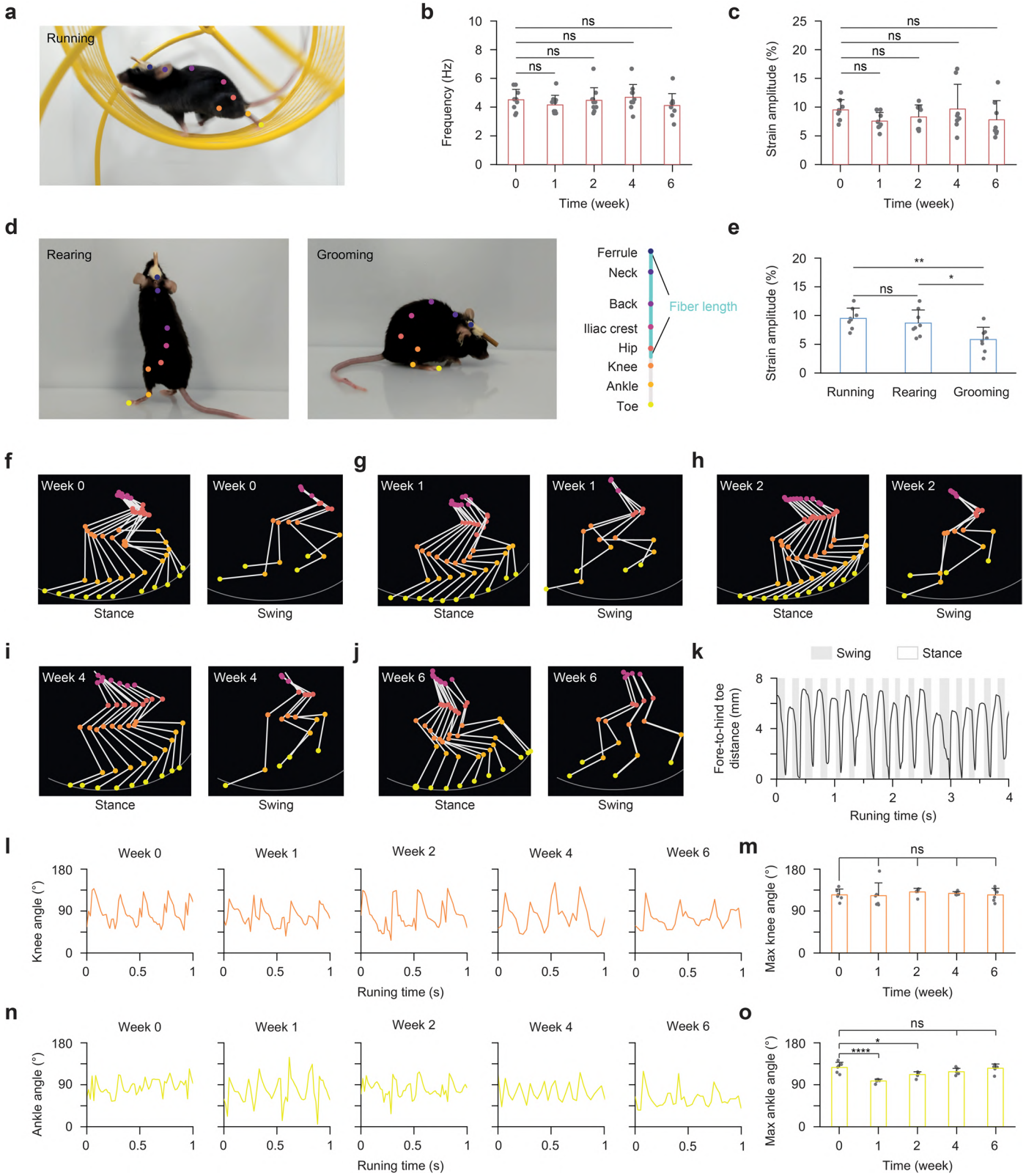
Extended Data Fig. 3 | Engineered optical performances of hydrogel fibers. **a**, Wide-angle X-ray scattering profiles for hydrogel core materials (dry state) with varied annealing times. **b**-**e**, Nanocrystalline domain size (b), refractive index (c), normalized absorbance at 473 nm (**d**), and normalized absorbance at 589 nm (e) for hydrogel core materials with varied annealing times. The dashed lines represent the values of PBS. AU: absorbance units. **f**, Attenuation coefficient at 473 nm for hydrogel fibers, in which the hydrogel core materials have varied annealing times. **g**, **h**, Crystallinity (g) and refractive index (h) for hydrogel core materials with varied glutaraldehyde (GA) amounts. The dashed line represents the refractive index of PBS. **i**, Attenuation coefficient at 473 nm for hydrogel fibers, in which the hydrogel core materials have varied GA amounts. **j**, **k**, Schematic (j) and ray tracing simulation (k) of hydrogel fibers, in which the hydrogel core materials have varied refractive indices. **l**-**m**, Representative plots of light intensity delivered through hydrogel fibers in PBS vs. tensile strain, in which the hydrogel core materials have varied annealing time. The right images show the hydrogel fibers (no cladding) at different tensile strains with two ends connected to a light source and a photodetector, respectively. Scale bars: 5 mm. **n**, Transmittance spectra for hydrogel cladding materials with varied reduction times and the hydrogel core material. **o**-**q**, Refractive index (o), normalized absorbance at 473 nm (p), and normalized absorbance at 589 nm (q) for hydrogel cladding materials with varied reduction times and the hydrogel core material. The dashed lines represent the values of PBS. AU: absorbance units. **r**, Attenuation coefficient at 473 nm for hydrogel fibers over time when incubated in the PBS at 37 °C. One-way ANOVA with Tukey's multiple comparison test. ns: not significant.

https://doi.org/10.1038/s41592-023-02020-9



Extended Data Fig. 4 | Engineered mechanical performances of hydrogel fibers. a, Representative plot of nominal stress vs. strain of the hydrogel fiber (without silica) under single-cycle tensile test. The measured tensile strength is 4.6 MPa and Young's modulus is 1.8 MPa. **b**, Plot of crack extension rate vs. energy release rate of the hydrogel core material (without silica) under cyclic tensile test. The measured fatigue threshold is 1,400 J m^{-2}. **c**, Plot of nominal stress vs. strain of the hydrogel fiber (with silica) under cyclic tensile test. The applied stress amplitude in the cyclic tensile test is 1.4 MPa and the cycle number is 10,000 and 30,000. The hysteresis for both stress-strain curves are 0%. **d**, Plot of strain vs. cycle number of the hydrogel fiber under cyclic tensile test. The applied stress amplitude in the cyclic tensile test is 1.8 MPa and the total cycle number (N_c) is 3,347. **e**, Microscopic images of the hydrogel fiber at different tensile stresses of 0 MPa and 1.8 MPa under cyclic tensile test. Cavitation happens at the hydrogel-silica interface when the applied stress amplitude is 1.8 MPa. Scale bars: 0.5 mm. **f**, Plot of applied stress amplitude vs. stretch cycle number to break of the hydrogel fiber (with silica), or the stress-life curve. The measured fatigue strength is 1.4 MPa. g-h, Tensile strength (**g**) and strain energy density (**h**) for hydrogel fibers over time when incubated in the PBS at 37 °C. **i**, Representative plot of normalized light intensity vs. bending radius of the silica, PDMS, and hydrogel fibers in PBS. **j**, **k**, Schematic and image of a hydrogel cuff (j) and a hydrogel membrane (k) at the optical fiber terminal attached to artificial tissues (nerve and heart). The inset is an image of the hydrogel cuff in the dark field with light on. One-way ANOVA with Tukey's multiple comparison test for g,h. ns: not significant.

https://doi.org/10.1038/s41592-023-02020-9

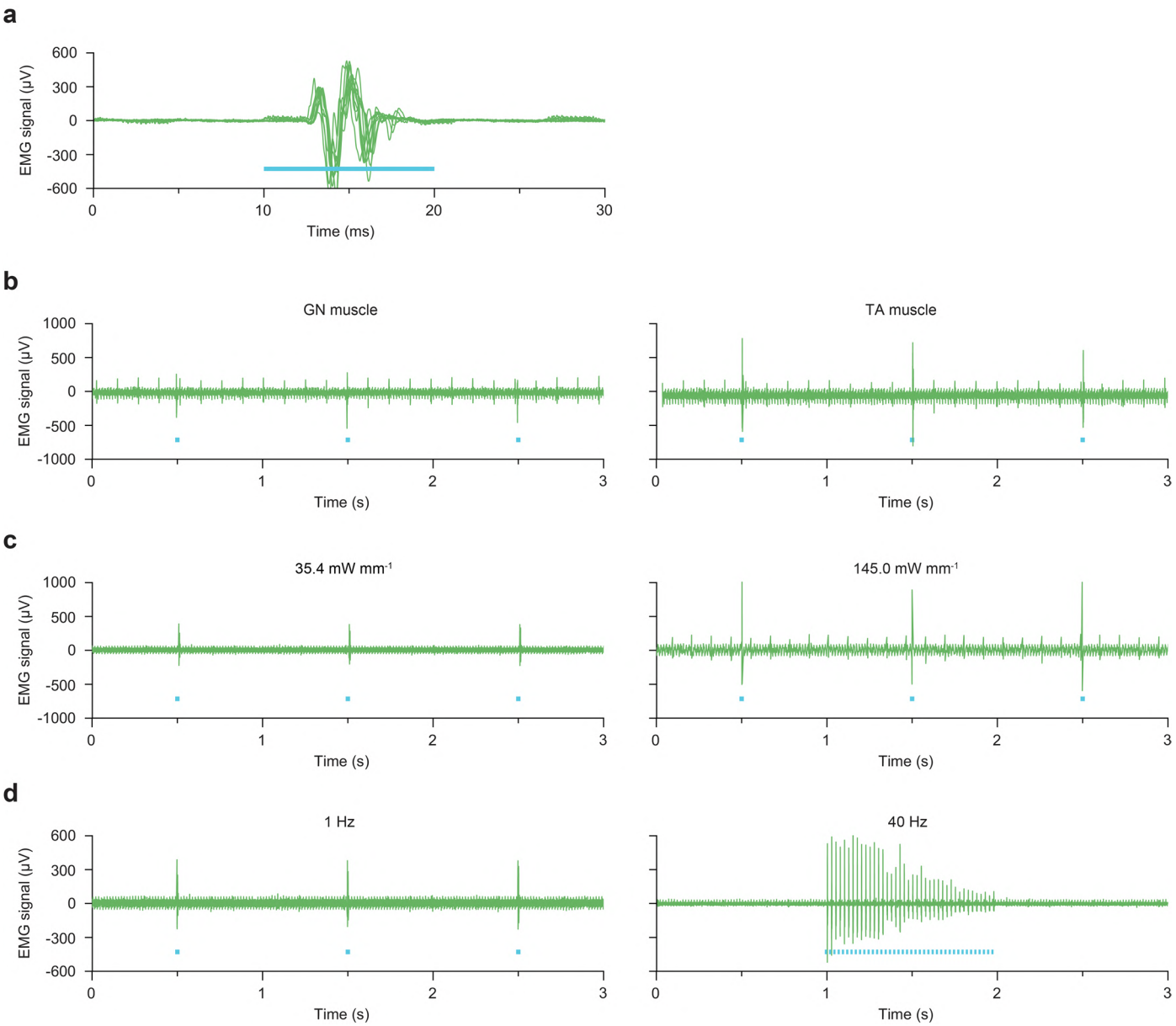


Extended Data Fig. 5 | See next page for caption.

https://doi.org/10.1038/s41592-023-02020-9

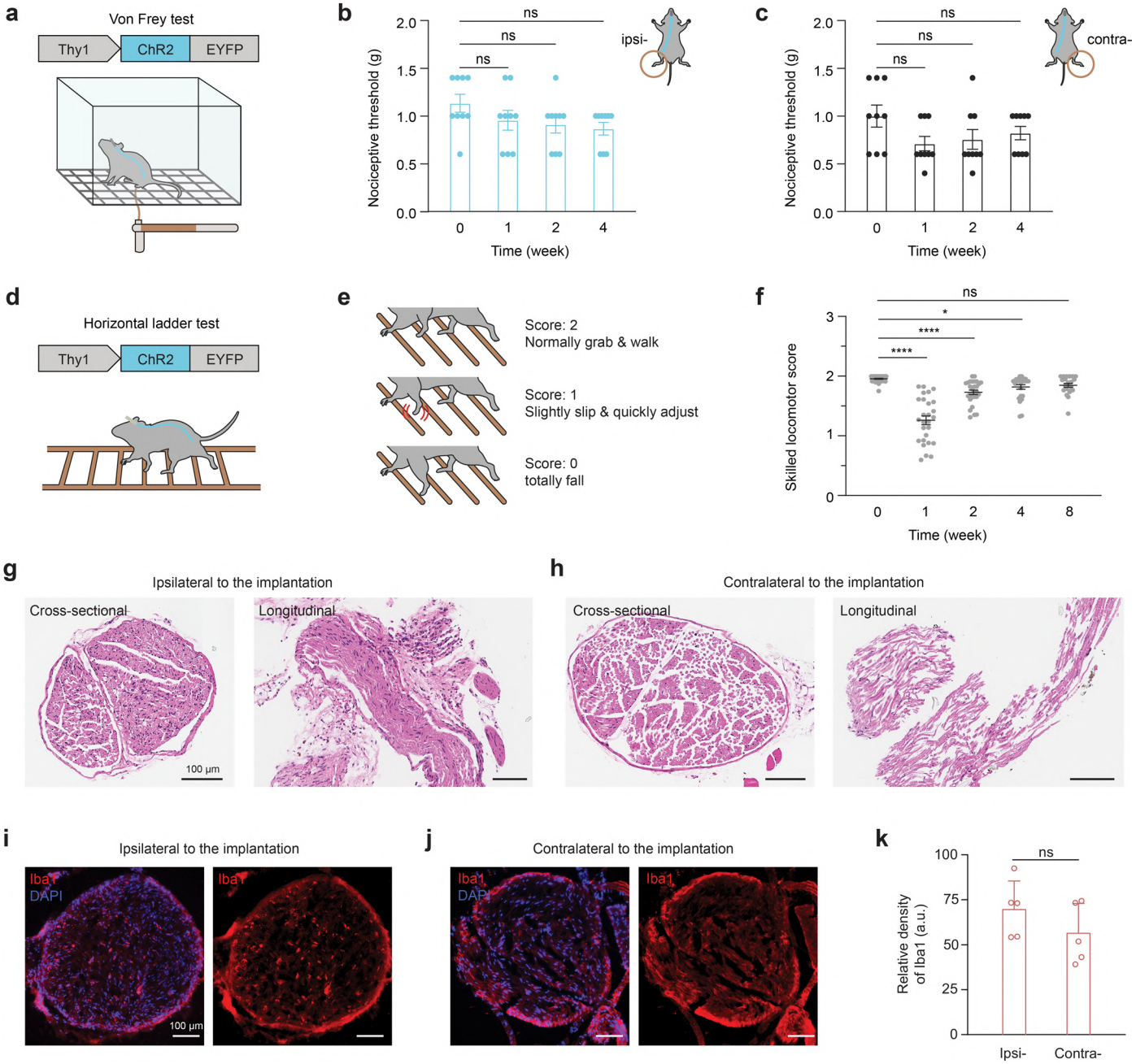
Extended Data Fig. 5 | Gait analysis of mice implanted with hydrogel fibers. **a**, Image of a mouse implanted with a hydrogel fiber moving on a running wheel. The mouse is labeled with nodes for the ferrule, neck, back, iliac crest, hip, knee, ankle, and toe. **b**, **c**, Frequency of gait cycle (that is, fiber stretch cycle, b) and strain amplitude of hydrogel fibers (c) during mice movement on a running wheel from week 0 to week 6. **d**, Images of a mouse rearing and grooming when implanted with a hydrogel fiber. The mouse is labeled with nodes for the ferrule, neck, back, iliac crest, hip, knee, ankle, and toe. The fiber length, highlighted in blue, is calculated by the total length of the segments starting from the ferrule to the middle point between the hip and knee. **e**, Quantified strain amplitude of hydrogel fibers during mice running, rearing, and grooming. **f**-**j**, Kinematic stick diagram of mouse hindlimb movement on a running wheel on week 0 (f) before implantation, and week 1 (g), week 2 (h), week 4 (i) and week 6 (j) after implantation. A gait cycle is composed of a stance phase (left) and a swing phase (right) in the kinematic stick diagram. The nodes represent the iliac crest, hip, knee, ankle, and toe from top to bottom. **k**, Representative plot of distance between the fore toe to hind toe over time during mice movement on a running wheel. The total time period is divided into a few gait cycles, and each cycle is discomposed to a swing phase and a stance phase according to the positive or negative slope. **l**, Representative plots of knee angle variation during mice hindlimb movement on a running wheel from week 0 to week 6. **m**, Quantified maximum knee angle during mice hindlimb movement on a running wheel from week 0 to week 6. **n**, Representative plots of ankle angle variation during mice hindlimb movement on a running wheel from week 0 to week 6. **o**, Quantified maximum ankle angle during mice hindlimb movement on a running wheel from week 0 to week 6. One-way ANOVA with Tukey's multiple comparison test for b,c,e,m,o. ns: not significant.

https://doi.org/10.1038/s41592-023-02020-9



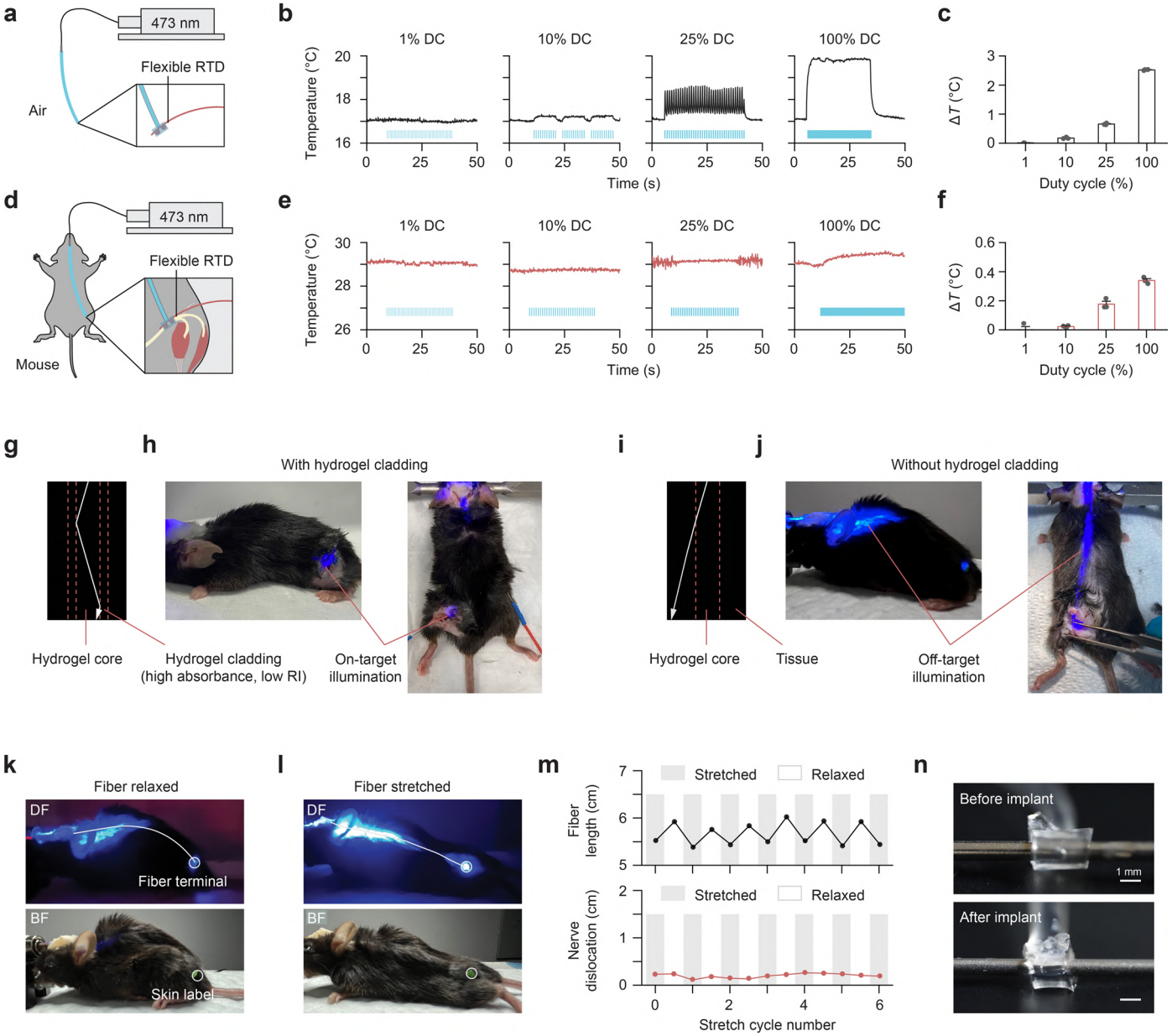
Extended Data Fig. 6 | Optogenetic stimulation measured by EMG signals. **a**, Overlay plot of EMG signals recorded on the GN muscle when the frequency of optical pulses is 1 Hz (ON: 10 ms, OFF: 990 ms) and the irradiance is 35.4 mW mm^{-2}. **b**, Plots of EMG signals recorded on the GN muscle (left) and TA muscle (right) when the frequency of optical pulses is 1 Hz and the irradiance is 35.4 mW mm^{-2}. **c**, Plots of EMG signals recorded on the GN muscle when the frequency of optical pulses is 1 Hz and the irradiance is 35.4 mW mm^{-2} (left) or 145.0 mW mm^{-2} (right). **d**, Plots of EMG signals recorded on the GN muscle when the frequency of optical pulses is 1 Hz (left) or 40 Hz (right), and the irradiance is 35.4 mW mm^{-2}. Blue bars indicate optical pulses from a 473-nm light source.

https://doi.org/10.1038/s41592-023-02020-9



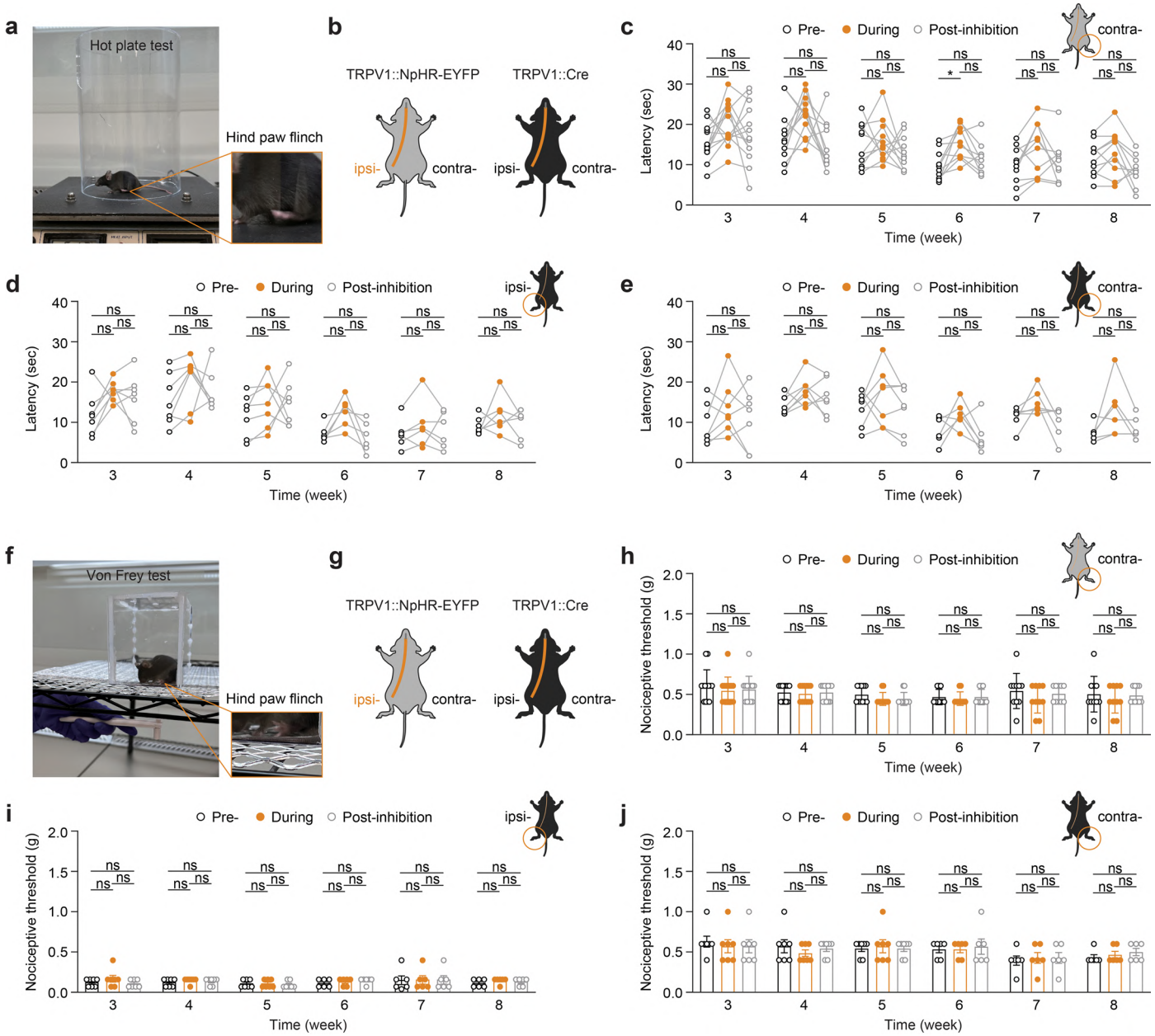
Extended Data Fig. 7 | Behavior and biocompatibility tests of mice implanted with hydrogel fibers. a, Schematic showing a Thy1::ChR2-EYFP mouse with a hydrogel fiber during von Frey tests. **b**, **c**, Nociceptive thresholds of ipsilateral (b) and contralateral (c) hind paw flinch in von Frey tests for Thy1::ChR2-EYFP mice over time after implantation. **d**, Schematic showing a Thy1::ChR2-EYFP mouse with a hydrogel fiber during horizontal ladder tests. **e**, Steps are counted and classified as either a normal walk (score 2), a slight slip (score 1), and a fall (score 0). **f**, Skilled locomotor score of ipsilateral hind paws for Thy1::ChR2-EYFP mice over time after implantation. **g**-**h**, Representative histological images of TRPV1::NpHR-EYFP mice's ipsilateral (g) and contralateral (h) sciatic nerves. Sciatic nerves were harvested 8 weeks after implantation, and stained using hematoxylin and eosin (H&E). Blue: cell nuclei by hematoxylin; pink: extracellular matrix and cytoplasm by eosin. Scale bars: 100 μm. **i**,**j**, Representative immunohistochemistry images of Thy1::ChR2-EYFP mice's ipsilateral (i) and contralateral (j) sciatic nerves. Sciatic nerves were harvested 8 weeks after implantation, and stained using anti-Iba1 antibodies for macrophages. Red: Iba1; blue: DAPI. Scale bars: 100 μm. **k**, Iba1 relative densities in both ipsilateral and contralateral sciatic nerves. ns: not significant.

https://doi.org/10.1038/s41592-023-02020-9



Extended Data Fig. 8 | Evaluation of optical illumination through implanted hydrogel fibers. a, Schematic of the temperature measurement through a resistance temperature detector (RTD) at the hydrogel cuff in air. The light source delivers 473-nm optical pulses with an irradiance of 35.4 mW mm^{-2}. **b**, Plots of temperature variation in air when the optical pulses exhibit different duty cycles (DCs). Blue bars indicate optical pulses. **c**, Temperature increase in air under optical pulses with different DCs. **d**, Schematic of the temperature measurement through an RTD at the hydrogel cuff in mice. The light source delivers 473-nm optical pulses with an irradiance of 35.4 mW mm^{-2}. **e**, Plots of temperature variation in mice when the optical pulses exhibit different DCs. Blue bars indicate optical pulses. **f**, Temperature increase in mice under optical pulses with different DCs. **g**, Ray tracing simulation of hydrogel fibers with the hydrogel cladding. **h**, Images of a mouse implanted with a hydrogel fiber with the hydrogel cladding, showing on-target illumination. **i**, Ray tracing simulation of hydrogel fibers without the hydrogel cladding. **j**, Images of a mouse implanted with a hydrogel fiber without the hydrogel cladding, showing off-target illumination. **k**-**l**, Darkfield (DF) and brightfield (BF) images of a mouse implanted with a hydrogel fiber (no cladding) when the fiber is relaxed (k) and stretched (l). Contours of the hydrogel fiber without cladding are visible in the darkfield. The skin on top of the sciatic nerve is labeled with a green sticker to identify the original sciatic nerve position. **m**, Change of fiber length and nerve dislocation over fiber stretch cycles. **n**, Images of the hydrogel cuff before and after 8-week implantation in mice.

https://doi.org/10.1038/s41592-023-02020-9



Extended Data Fig. 9 | Optogenetic inhibition of nociception in naturally behaving mice enabled by hydrogel fibers (control and contralateral). a, Image of the experimental setup for hot plate tests, during which animal hind paw flinches were observed. **b**, Schematic of TRPV1::NpHR-EYFP mice (test group) and TRPV1::Cre mice (control group) with ipsilateral and contralateral hind paws. Yellow optical pulses were applied with a pulse width of 25 ms and irradiance of 8.5 mW mm^{-2}. **c**, Latency of first-time contralateral hind paw flinch in hot plate tests for TRPV1::NpHR-EYFP mice over time after implantation. **d**, Latency of first-time ipsilateral hind paw flinch in thermal nociception tests for TRPV1::Cre mice over time after implantation. **e**, Latency of first-time contralateral hind paw flinch in thermal nociception tests for TRPV1::Cre mice over time after implantation. **f**, Image of the experimental setup for von Frey tests, during which animal hind paw flinch were observed. **g**, Schematic of TRPV1::NpHR-EYFP mice (test group) and TRPV1::Cre mice (control group) with ipsilateral and contralateral hind paws. Yellow optical pulses were applied with a pulse width of 25 ms and irradiance of 8.5 mW mm^{-2}. **h**, Nociceptive threshold of contralateral hind paw flinch in von Frey tests for TRPV1::NpHR-EYFP mice over time after implantation. **i**, Nociceptive threshold of ipsilateral hind paw flinch in von Frey tests for TRPV1::Cre mice over time after implantation. **j**, Nociceptive threshold of contralateral hind paw flinch in von Frey tests for TRPV1::Cre mice over time after implantation. ns: not significant.

nature portfolio

Corresponding author(s): Xinyue Liu, Siyuan Rao, Polina Anikeeva, Xuanhe Zhao

Last updated by author(s): Jul 6, 2023

Reporting Summary

Nature Portfolio wishes to improve the reproducibility of the work that we publish. This form provides structure for consistency and transparency in reporting. For further information on Nature Portfolio policies, see our Editorial Policies and the Editorial Policy Checklist.

Statistics

For all statistical analyses, confirm that the following items are present in the figure legend, table legend, main text, or Methods section.

n/a	Confirmed
☐	☒ The exact sample size (*n*) for each experimental group/condition, given as a discrete number and unit of measurement
☐	☒ A statement on whether measurements were taken from distinct samples or whether the same sample was measured repeatedly
☐	☒ The statistical test(s) used AND whether they are one- or two-sided *Only common tests should be described solely by name; describe more complex techniques in the Methods section.*
☐	☒ A description of all covariates tested
☐	☒ A description of any assumptions or corrections, such as tests of normality and adjustment for multiple comparisons
☐	☒ A full description of the statistical parameters including central tendency (e.g. means) or other basic estimates (e.g. regression coefficient) AND variation (e.g. standard deviation) or associated estimates of uncertainty (e.g. confidence intervals)
☐	☒ For null hypothesis testing, the test statistic (e.g. *F*, *t*, *r*) with confidence intervals, effect sizes, degrees of freedom and *P* value noted *Give P values as exact values whenever suitable.*
☒	☐ For Bayesian analysis, information on the choice of priors and Markov chain Monte Carlo settings
☒	☐ For hierarchical and complex designs, identification of the appropriate level for tests and full reporting of outcomes
☒	☐ Estimates of effect sizes (e.g. Cohen's *d*, Pearson's *r*), indicating how they were calculated

Our web collection on statistics for biologists contains articles on many of the points above.

Software and code

Policy information about availability of computer code

Data collection	-We performed kinematic analysis on the recorded animal natural behaviors using a markerless pose estimation software (DeepLabcut). -We performed ray tracing simulations in the optical fibers by using Ray Optics Simulation (https://phydemo.app/ray-optics/simulator/).
Data analysis	-Statistical analyses were performed in GraphPad Prism 9 and OriginPro 2023. We first performed Shapiro-Wilks tests for data normality. For independent data with normal distribution, we used one-way ANOVA with Tukey's multiple comparison test. For independent data with non-normal distribution, we used Kruskal-Wallis ANOVA with Dunn's multiple comparison test. For paired data with normal distribution, we used one-way repeated measures ANOVA with Tukey's multiple comparison test. For paired data with non-normal distribution, we used Friedman tests with Dunn's multiple comparison test. -We used a custom algorithm written in MATLAB R2019b to determine a single gait cycle in VWRTs between two local minimums in the plot of distance between the fore toe to hind toe over time, and divided into the swing phase and stance phase during VWRTs. -We used a custom algorithm written in Python3.9.1 to score mouse horizontal ladder walking behaviors. -Data analysis in the manuscript: Statistical analyses were performed in GraphPad Prism 9 and OriginPro 2023. We first performed Shapiro-Wilks tests for data normality. For independent data with normal distribution, we used one-way ANOVA with Tukey's multiple comparison test. For independent data with non-normal distribution, we used Kruskal-Wallis ANOVA with Dunn's multiple comparison test. For paired data with normal distribution, we used one-way repeated measures ANOVA with Tukey's multiple comparison test. For paired data with non-normal distribution, we used Friedman tests with Dunn's multiple comparison test. P values less than 0.05 were considered significant: *0.01 ≤P<0.05, **0.001≤P<0.01, **0.001≤P<0.01, ****P<0.0001. The detailed statistical information for Figures, Extended Data Figures, and

Supplementary Figures are indicated in the Supplementary Tables 2–21.

-Data Availability stated in the manuscipt: The data associated with this study are available in the article and the Supplementary Information. Source data are provided with this publication. In addition, the original data of material characterization, optogenetic stimulation, biocompatibility test, behavior test, and pain inhibition have been deposited in the public repository Figshare (https://figshare.com) and are accessible at https://doi.org/10.6084/m9.figshare.c.6703152.v3.

For manuscripts utilizing custom algorithms or software that are central to the research but not yet described in published literature, software must be made available to editors and reviewers. We strongly encourage code deposition in a community repository (e.g. GitHub). See the Nature Portfolio guidelines for submitting code & software for further information.

Data

Policy information about availability of data

All manuscripts must include a data availability statement. This statement should provide the following information, where applicable:

- Accession codes, unique identifiers, or web links for publicly available datasets
- A description of any restrictions on data availability
- For clinical datasets or third party data, please ensure that the statement adheres to our policy

The data associated with this study are available in the article and the Supplementary Information. Source data are provided with this publication. In addition, the original data of material characterization, optogenetic stimulation, biocompatibility test, behavior test, and pain inhibition have been deposited in the public repository Figshare (https://figshare.com) and are accessible at https://doi.org/10.6084/m9.figshare.c.6703152.v3.

Human research participants

Policy information about studies involving human research participants and Sex and Gender in Research.

Reporting on sex and gender	N/A
Population characteristics	N/A
Recruitment	N/A
Ethics oversight	N/A

Note that full information on the approval of the study protocol must also be provided in the manuscript.

Field-specific reporting

Please select the one below that is the best fit for your research. If you are not sure, read the appropriate sections before making your selection.

☒ Life sciences ☐ Behavioural & social sciences ☐ Ecological, evolutionary & environmental sciences

For a reference copy of the document with all sections, see nature.com/documents/nr-reporting-summary-flat.pdf

Life sciences study design

All studies must disclose on these points even when the disclosure is negative.

Sample size	Sample sizes for behavioral experiments were informed by the number of subjects reported for similar studies, based on the minimal number of mice required to detect significance in a standard power experiment. Charaterization of hydrogel materials. 3-4 independent samples. Charaterization of hydrogel optical fibers. 3-4 independent samples. In vivo implantation of hydrogel optical fibers. Thy1::ChR2-EYFP (n = 15), TRPV1::NpHR-EYFP (n = 13), and TRPV1::Cre (n = 7) mice were implanted with hydrogel optical fibers. Voluntary wheel running tests. Thy1::ChR2-EYFP mice (n = 6) with implanted hydrogel optical fibers were subjected to VWRTs during weeks 0–8 following surgery. Optogenetic stimulation in mice. Thy1::ChR2-EYFP mice (n = 6) with implanted hydrogel optical fibers were subjected to optogenetic stimulation during weeks 0–8 following surgery. Evaluation of skilled locomotion using horizontal ladder tests. Thy1::ChR2-EYFP mice (n = 9) with implanted hydrogel optical fibers were subjected to horizontal ladder tests during weeks 0–8 following surgery.

Induction and maintenance of inflammatory pain. TRPV1::NpHR-EYFP (n = 13) and TRPV1::Cre (n = 7) mice with implanted hydrogel optical fibers were subjected to CFA and IFA injections.

Evaluation of mechanical sensitivity using von Frey tests. Thy1::ChR2-EYFP (n = 9) mice with implanted hydrogel optical fibers were subjected to von Frey tests during weeks 0–4 following surgery, and TRPV1::NpHR-EYFP (n = 13) and TRPV1::Cre (n = 7) mice with implanted hydrogel optical fibers were subjected to von Frey tests during weeks 0–8 following surgery.

Evaluation of thermal sensitivity using hot plate tests. TRPV1::NpHR-EYFP (n = 13) and TRPV1::Cre (n = 7) mice with implanted hydrogel optical fibers were subjected to hot plate tests during weeks 0–8 following surgery.

Optogenetic inhibition of nociception in naturally behaving mice. ... TRPV1::NpHR-EYFP mice (week 3, n = 13; week 4, n = 12; week 5, n = 11; week 6–8, n = 10) in the test group and TRPV1::Cre mice (week 3–5, n = 7; week 6–8, n = 6) in the control group were subjected to optogenetic inhibition during weeks 0–8 following surgery.

Data exclusions

3 TRPV1::NpHR mice (test group) and 1 TRPV1::Cre mouse (control group) were excluded because of accidental device damage during operations.

Replication

All attempts at replication were successful for the experiments are listed.

In von Frey tests, each monofilament was applied ten times, and the number of immediate hind paw flinch to each force was recorded. The force at which the paw flinch occurred at least six times was considered as the nociceptive threshold.

In light intensity measurement of hydrogel fibers, each measurement was repeated three times.

Randomization

Since the study goals is to validate the light delivery functionality of hydrogel fibers and prior to, during, and post light stimualtion conditions have been considered, randomization of animals is not applicable for this study goal. Different mice (ChR2, NpHR, Cre) were known throughout the experiments and analysis.

Blinding

A separate naive group of blinded investigators conducted data analysis, including hot plate tests and horizontal ladder walk tests. Because the study goal is to validate the light transmission functionality and different conditions (before, during and after light stimulation) have been include, the investigators were not blinded during optogenetic stimulation nor behavior data collection.

Reporting for specific materials, systems and methods

We require information from authors about some types of materials, experimental systems and methods used in many studies. Here, indicate whether each material, system or method listed is relevant to your study. If you are not sure if a list item applies to your research, read the appropriate section before selecting a response.

Materials & experimental systems

n/a	Involved in the study
☐	☒ Antibodies
☒	☐ Eukaryotic cell lines
☒	☐ Palaeontology and archaeology
☐	☒ Animals and other organisms
☒	☐ Clinical data
☒	☐ Dual use research of concern

Methods

n/a	Involved in the study
☒	☐ ChIP-seq
☒	☐ Flow cytometry
☒	☐ MRI-based neuroimaging

Antibodies

Antibodies used

anti-GFP antibody (Abcam ab13970), Alexa Fluor 488 (Invitrogen A-11039), rabbit mAb anti-Iba1 (Abclonal A19776, CloneNo. ARC2301), Alexa Fluor 568 (Invitrogen A- 10042)

Validation

manufactures' website and references(Immunofluorescence analysis of mouse brain using AIF1/AIF1/IBA1 Rabbit mAb (A19776) at dilution of 1:100 (40x lens). Blue: DAPI for nuclear staining; https://abclonal.com/catalog-antibodies/AIF1IBA1RabbitmAb/A19776)

Animals and other research organisms

Policy information about studies involving animals; ARRIVE guidelines recommended for reporting animal research, and Sex and Gender in Research

Laboratory animals

Adult (>8 weeks) Thy1::ChR2-EYFP, TRPV1::Cre, LoxP-NpHR mice were originally purchased from the Jackson Laboratory and bred at MIT and UMass Amherst.
Thy-ChR2 mice, male and female, age from 9 weeks to 66 weeks
TRPV1-Cre mice, male and female, 11 weeks
TRPV1-NpHR mice, 14 weeks

	Thy1::ChR2-EYFP mice were bred by the Division of Comparative Medicine (DCM) at MIT and UMass Amherst. TRPV1::Cre and LoxP-NpHR mice were genetically crossed to breed TRPV1::NpHR mice at UMass Amherst.
Wild animals	No wild animals were used in the study
Reporting on sex	Both sexes
Field-collected samples	No field collected samples were used in the study.
Ethics oversight	MIT American Association for Laboratory Animal Science (IACUC) and Division of Comparative Medicine (DCM) , UMass Amherst IACUC

Note that full information on the approval of the study protocol must also be provided in the manuscript.